Crustal and upper mantle density variations beneath the western U.S.: compositional topography, thermal topography, and gravitational potential energy

Will Levandowski[1], Craig H. Jones[1], Weisen Shen[2], Michael H. Ritzwoller[2], and Vera Schulte-Pelkum[1]
1 - Cooperative Institute for Research in Environmental Sciences and Department of Geological Sciences, University of Colorado at Boulder, Boulder, CO 80309-0390
2- Department of Physics, University of Colorado at Boulder, Boulder, CO 80309-0390

Abstract

To investigate the physical basis for support of topography in the western U.S., we construct a sub-continent scale, 3D density model using ~1000 estimated crustal thicknesses and *S*-velocity profiles to 150 km depth at each of ~1000 seismic stations. Seismic signatures of temperature and composition are considered in the crust, but we assume that mantle velocity variations are thermal in origin. From these densities, we calculate crustal and mantle topographic contributions. Typical 2σ uncertainty of topography is ~590 meters; elevations in 84% of the region are reproduced within error. Remaining deviations are attributed to melt, large variations in crustal quartz content, and dynamic topography. Support for western U.S topography is heterogeneous, with each province having a unique combination of mechanisms. Topography due to mantle buoyancy is nearly constant (within ~250 m) across the Cordillera; relief is dominated by variations in crustal chemistry and thickness (>2 km). Cold mantle provides ~1.5 km of ballast to the thick crust of the Great Plains and Wyoming craton. Crustal temperature variations and dynamic pressures have smaller magnitude and/or more localized impacts. We also calculate the gravitational potential energy (GPE) from our density model. Positive GPE anomalies (~$2x10^{12}$N/m) promote extension in the northern Basin and Range and near the Sierra Nevada. Negative GPE anomalies ($-3x10^{12}$N/m) along the western North American margin and Yakima fold and thrust belt add compressive stresses. We thus argue that stresses derived from lithospheric density variations dominate edge and basal force-derived stresses in many regions in the western U.S. continental interior.

1. Introduction

The Cordilleran orogen of the western United States is one of the broadest on Earth. Elevations above 1 km extend 1500 km from the plate boundary (Figure 1a) and active deformation extends 1000 km from the plate boundary. Unlike other relatively broad boundaries, this orogen lacks a continental collision or even subduction over much of its length. The processes producing such widespread uplift and deformation remain poorly understood largely because of the heterogeneous history of different parts of the orogen and the absence of uniformly collected and analyzed orogen-scale information on the crustal and upper mantle structure of the region. We address this deficiency through analysis of newly created seismic wavespeed models of this region developed from ambient noise and earthquake surface wave tomography that has yielded crustal and upper mantle structures at EarthScope Transportable Array (TA) stations spaced roughly every 80 km throughout the region.

Variations in continental elevation stem from some combination of variations in crustal density, crustal thickness, mantle density and basal normal stress at the model bottom, to the last of which we apply the unevenly defined term "dynamic topography." The mantle component of topography arises from variations in the density and thickness of the mantle lithosphere. Variations in the thickness of crust and mantle lithosphere are generally products of tectonism, whereas variations in densities are often the results of magmatism and thermal adjustments that can occur during more tectonically quiescent times. Thus isolating the modern day elements of support for regions within the western U.S. also contributes towards our understanding of the origins of those elements.

At the broadest scale, the elevation of the orogen is often attributed to a warm and buoyant mantle [e.g. *Grand and Helmberger*, 1984] emplaced after removal of the lower lithosphere because of "flat slab" subduction during the 75-45 Ma Laramide orogeny [e.g., *Bird*, 1988; *Spencer*, 1996; *Humphreys*, 2009]. Many problems challenge this model, from disagreements over the geometry of the Laramide-age slab [e.g., *Sigloch and Mihalynuk*, 2013; *Saleeby*, 2003] through the post-Laramide presence of pre-Laramide mantle lithosphere in the western U.S. [e.g., *Livaccari and Perry*, 1993; *Ducea and Saleeby*, 1996] to the puzzling >1 km elevations of the untectonized High Plains [*Eaton*, 1986]. As a result, many workers have chosen to focus on pieces of the orogen, introducing a broad range of mechanisms for surface uplift of portions of the region. In the Colorado Plateau, for example, Roy et al. [2009] argue that ~2 km of Cenozoic surface uplift is due to conductive warming of the lithosphere, Levander et al. [2011] attribute elevation change to delamination of the lower crust and mantle lithosphere, and Moucha et al. [2008] favor dynamic support from the mantle convective regime. Such subregional studies often lack a regional framework that would contextualize and substantiate their hypotheses. We seek to provide such a framework and illustrate its application with specific examples.

The presence of Pleistocene to Recent deformation ~1000 km from the Pacific plate potentially shares a common origin with topography. The variations in stress manifest in observed strain are typically attributed to lateral variations in gravitational potential energy that arise from lateral variations in the thickness, elevation, and density of the lithosphere [e.g., *Flesch et al.*, 2007; *Flesch et al.*, 2000; *Humphreys and Coblentz*, 2007; *Sonder and Jones*, 1999], although the significance of the stresses generated by GPE variations has been disputed [*Parsons and Thatcher*, 2011]. Previous estimates of GPE (and thus the stresses that arise from lateral GPE variations) relied either on compiling and interpolating between seismic models produced by different techniques and then converting such structures into density or on filtering geoid anomalies. Geoid anomalies are equivalent to GPE if all the density anomalies contributing to the geoid are within the depth range appropriate for GPE calculations [*Haxby and Turcotte*, 1978]. In the western U.S., however, a long wavelength contribution is probably sublithospheric, so most workers filter the geoid. While removing the deeper contributions, filtering will also remove longer wavelength shallow contributions. Compiling seismic models in the literature and converting these to GPE estimates (e.g., Jones et al., 1996) carries the risk that biases between different workers and techniques will create geographic biases in GPE estimates. For many geodynamic applications, these discrete seismic models must be interpolated in some manner (e.g., CRUST 2.0, as used, for instance, by Flesch and Kreemer [2010]) that can further amplify biases and errors. A uniformly calculated estimate of GPE derived from an evenly distributed set of seismic observations would, at minimum, reduce any intra-orogenic uncertainty due to these biases.

The motivation for this work is to leverage the passage of Transportable Array (TA) seismometers across the western U.S. (Figure 1a) and the development of new seismic techniques [*Shen et al.*, 2013b] to produce a spatially pseudo-uniform 3D density model across the entire western U.S.. The suite of accepted velocity models (detailed below) provided by Shen et al. [2013a] removes inter-investigator biases while providing a robust measure of seismological uncertainty. In turn, the envelope of densities estimated from those velocities allows us to quantify the mechanisms of modern topographic support and decompose this field into crustal and mantle or thermal and compositional components. Finally, the density estimates consistent with topography and seismic velocities determine variations in the body forces that contribute to the modern stress field. This workflow overcomes many of the challenges faced in previous studies, which had to rely upon spatially variable data coverage, non-uniform data processing techniques, and models that may be highly dependent on the chosen inversion parameters.

Such an improved model set allows us to pursue answers to technically and geodynamically important questions. Can seismic velocities, in concert with heat flow measurements, be used to reliably estimate densities? We check our density estimates quantitatively against predicted topography and gravity. Where do these predictions fail? We examine regions where dynamic topography, crustal melt, and anomalously felsic crust are likely. To what extent are thermal, compositional and dynamic topography each responsible for surface elevations, and is one dominant? We decompose the elevation field into these components. What are the magnitudes of GPE variations in the western U.S., and how do these variations compare with modern strain? We quantify the GPE with respect to the asthenosphere throughout the region.

2. Seismic Models

Until recently, seismic structures available for the western U.S. presented serious difficulties when deriving contributions to topography from crust and mantle. Ideally, models would be based upon observations gathered uniformly that could distinguish wavespeeds in the crust from those in the mantle, as the relationship of wavespeed to density differs in the two layers. Active-source profiles are scattered erratically and interpretations, particularly of secondary arrivals, frequently differ between different workers (e.g., contrast Holbrook [1990] with Catchings and Mooney [1991], or Prodehl [1979] with Wolf and Cipar [1993]). These models rarely extend into the mantle lithosphere. Surface wave models have more uniformly sampled the lithosphere in this region with the deployment of the TA, but tradeoffs between wavespeeds of the crust and mantle are typically large. Local earthquake tomography is possible only where events occur and typically has poor resolution at depths in the upper mantle and lower crust below the deepest events. Teleseismic body-wave tomography and receiver functions recover only lateral gradients or contrasts and not absolute values and typically contain little information within the crust.

The shear-wavespeed structures of Shen et al. [2013a] permit derivation of lithospheric densities and associated uncertainties with a spatial density and uniformity down to wavelengths (~100 km) comparable to the shortest wavelength where variations in isostatic support are apt to be significant. At each of the ~1000 TA stations in the western U.S., Shen et al. (2013a) began with a loosely constrained prior distribution of seismic V_{SV} velocities with depth and derived posterior distributions of ~1000 shear-wave velocity profiles (0-150 km) and crustal thicknesses (Figure 1b) that jointly satisfy surface wave dispersion curves and receiver functions. The inclusion of receiver function constraints greatly improves depth resolution of velocities when compared to surface wave dispersion simulations alone [*Shen et al.*, 2013b].

Because Shen et al. (2013a) produce a distribution of posterior models that satisfy the original observations, we can properly account for the effect of uncertainty in the seismological models on the derived density profile. Previous work often relied on forward modeling of seismic travel-time observations lacking formal estimates of uncertainty. Additionally, because wavespeed structures intrinsically carry trade-offs between different depths (that is, uncertainties at one depth will covary with those at other depths), by estimating derived parameters (such as mean density) for each individual structure and then calculating the uncertainty in the derived parameter, we avoid overestimating the uncertainties arising from the seismological uncertainties. As explained in greater detail in section 4, we find that this seismological uncertainty dominates the uncertainty in our predicted topography, exceeding the uncertainty from the scatter in velocity to density regressions (Figure 2).

3. Density Estimation and Decomposition of Topography

We investigate the source of topographic relief in the western U.S. by exploiting the relationship between wavespeed and density. It is useful to separate the contribution to topography (e) from the crust (H_c) from that from the mantle (H_m). In this, we follow Lachenbruch and Morgan [1990] and define the following:

$$\varepsilon = H_c + H_m - H_0 \qquad (1)$$

where the crustal and mantle contributions to buoyant height are

$$H_c = \int_{-\varepsilon}^{z_c} \frac{\rho_a - \rho(z)}{\rho_a} dz$$
$$H_m = \int_{z_c}^{z_a} \frac{\rho_a - \rho(z)}{\rho_a} dz \qquad (2)$$

H_0 is a correction term of 2.4 km to achieve isostatic equilibrium with an asthenospheric column (via mid-ocean ridges). z is positive downward, such that the depth of the Moho below sea level is z_c. We assume the asthenosphere to be laterally uniform below the base of the seismic models (z_a) at 150 km. The density of the asthenosphere, ρ_a, is assumed to be 3200 kg/m^3. Because the motivation of this study is to explore the source of topographic variation in the region, the exact choice of reference asthenospheric density is of second-order importance. As in earlier studies (e.g., Jones et al., 1996), we suppress flexurally supported topography by smoothing by convolution with a zero-order Bessel function [*Watts*, 2001] based on elastic thickness estimates (Figure 1c) [*Lowry et al.*, 2000; *Lowry*, 2012] to estimate ε, the isostatically supported elevation above sea level. By doing so, we examine the topography that must be supported by lateral density variations rather than by elastic strength.

In order to calculate H_m and H_c, at each point we convert each of the ~1000 member distribution of v_s models into a density profile. Separating the support for smoothed topography into crustal and mantle components is necessary because we use different approaches in crust and mantle to derive densities from seismic wavespeeds. The crustal and mantle topographic contributions are smoothed by the same flexural filter described above.

3.1 Mantle-supported topography

We initially solve for H_m (which we will term the mantle topography for clarity) by assuming that density and wavespeed variations are a product of thermal heterogeneity. Isobaric heating will produce a decrease in both density and seismic velocity. Over a wide variety of lherzolite, harzburgite and peridotite mineralogies the temperature derivative of density is nearly the same, though the absolute densities vary considerably [*Hacker and Abers*, 2004]. Therefore, we make no initial assumption of mantle mineralogy other than that it is laterally constant across the study area at any depth. Using a compositionally independent conversion of velocity anomalies to density anomalies, we can then constrain the mantle contributions to isostasy for a purely thermally varying mantle, interpreting *S*-wavespeed variations reported by Shen et al. [2013a] as temperature variations and calculating the resulting density structure.

Laboratory data [*Jackson and Faul*, 2010] show a non-linear dependence of shear modulus on temperature, particularly within 150-200 °C of the solidus. To account for increasing anelastic effects with increasing temperature, we must relax the linear relationship between density and velocity at low velocities (Figure 3). Between 0% and -3% velocity anomaly (with respect to v_s=4.5 km/s, justified below), estimated $\partial\rho/\partial v_s$ decreases from 7 to 5 kg/m^3 per 1% velocity anomaly. This choice of parameters simulates the behavior of millimeter-scale single crystal grains of olivine [*Jackson and Faul*, 2010]. We assume that velocity anomalies beyond -3% are due to melt (~150 °C temperature perturbation relative to velocity anomaly of 0%, v_s=4.5 km/s). Since melt produces small changes in bulk density (between 0 and 4 kg/m^3 per 1% in situ melt fraction) [e.g., *Hammond and Humphreys*, 2000], we assume that density is constant for wavespeed anomalies less than -3%. If the solidus lies at a temperature of 1350 °C, then a 0% velocity anomaly represents a temperature of 1200 °C.

This estimate can be supported by comparing seismic velocities [from *Shen et al.*, 2013a] with temperature estimates at depth. The maximum velocity found by Shen et al. (2013a) at 120 km depth is 4.75 km/s and is observed in the Wyoming craton. Here, the thermal boundary layer is ~200 km thick [e.g., *Schutt et al.*, 2011], and thus, if the geotherm is approximately linear, the expected temperature at 120 km depth is ~820 °C (surface temperature 20 °C). The seismic velocity anomaly (+5.6%) represents a ~380 °C temperature decrease relative to material with no anomaly (and thus with a velocity of 4.5 km/s). From this, we would calculate that velocities of 4.5 km/s are associated with temperature of ~1200 °C, in agreement with our assumption made above.

We assume that there is no variation with depth of our velocity to density relationship largely because of uncertainty in the depth variation of anelastic effects. Certainly the solidus occurs at increasingly lower velocities at greater depth, but the volume of material affected is small and has little effect on our calculations. Errors in this approximation might yield errors in our estimate of topography of up to about 200m.

We assume that mantle loads are fully coupled to the overlying crust and surface. The degree to which loads present in a deforming viscous medium affect surface topography depends on the viscosity structure of the medium and load wavelength [e.g., *Parsons and Daly*, 1983]. Nevertheless, the lateral resolution (~100 km) of dispersion curve inversions and long wavelength (200-300 km) of velocity anomalies reported by Shen et al. [2013a] are great enough that we treat mantle loads as fully coupled to the surface. We then smooth these values by the estimated flexural response of the lithosphere. Following these assumptions, we calculate the mantle topography (Figure 4a).

3.2 Crust-supported topography

We assume that seismic wavespeeds in the crust depend on some combination of composition and temperature. We convert *S*-wavespeeds to density within the crust using Brocher's [2005] regression of density onto *S*-wavespeed and a correction for thermal variations based on estimates of temperature variations in the crust, discussed below.

The assumption of an isothermal crust would maximize estimates of crustal density variations, as the partial derivatives $\partial\rho/\partial v_{s(temperature)}$ and $\partial\rho/\partial v_{s\ (composition)}$ are different.

Regressions of density onto velocity [*Brocher*, 2005; *Christensen*, 1996] show that near 3.5 km/s and 2800 kg/m^3, $\partial\rho/\partial v_{s\ (composition)} \approx$ 544 kg/m^3 per km/s, while $\partial\rho/\partial v_{s\ (temperature)}$=249.2 kg/m^3 per km/s, assuming a coefficient of thermal expansion of 2.5×10^{-5} °C^{-1}, a v_p/v_s of 1.78 that is insensitive to temperature, and a $\partial v_p/\partial T$ of -0.5 m/s per °C [*Christensen and Mooney*, 1995]; this calculation is discussed below. Because of this difference, and because we aim to quantify the tectonic significance of crustal temperature variation, we seek to separate the minor (-0.281 m/s °C^{-1}) velocity (and thus inferred density) variations due to temperature from those due to composition, and to do so we must estimate the mean temperature of the crust.

We limit the mean thermal perturbation to a range of ±250 °C. Note first that for a 200 km thermal boundary layer with a linear geotherm, 50 km thick crust, and 20 °C surface temperature, the temperature at the Moho would be ~350 °C. At the opposite end, the upper limit on Moho temperature is that of convecting asthenosphere, ~1350 °C. Thus the coldest crustal column has an average temperature anomaly of 500 °C throughout the crust relative to a column in contact with asthenosphere if geotherms are approximately linear.

We use surface heat flow observations (from SMU Geothermal Database; http://smu.edu/geothermal/georesou/DataRequest.asp, accessed on 11/15/2012) smoothed over a 100 km radius as a proxy for crustal temperature (Figure 4c). Obviously such a dataset places only some constraints on the overall thermal structure of the crust as hydrological effects, varying thermal conductivity, variable radioactive heat generation and disequilibrium geotherms all will disrupt the relationship between surface heat flow and subsurface thermal structure. We follow Hasterok and Chapman [2007a] and avoid any attempt to correct for these issues as observational constraints on all of these parameters are weak and spatially irregular. We instead assume a simple linear geotherm through the crust and a default Moho temperature intermediate between the two extremes described above: 850 °C. We propose that upper and lower 0.15 quantiles of heat flow, above 90 mW/m^2 and below 51 mW/m^2, respectively, represent the maximum thermal perturbations, meaning that variations outside this range represent more local irregularities in thermal parameters. For heat flow less than 51 mW/m^2, we assume a mean crustal temperature anomaly of -250 °C. The estimate then scales linearly with heat flow to a maximum perturbation of 250 °C at a heat flow of 90 mW/m^2. This *ad hoc* estimate is expressed mathematically as:

$$\Delta\bar{T}_{\text{crust}} = 250°\text{C}\frac{F-70.5}{19.5} \tag{3}$$

where F is the range-limited heat flow in mW/m^2. This approximation is adequate for our purpose owing both to the unknowns in the thermal structure and the relatively small contribution to topography from thermal variations within the crust, which, as we discuss below, has a total range of about 700 m (Figure 4e).

Our estimate of crustal density is thus derived from our inferred temperature variation and the observed shear wavespeed:

$$\begin{aligned}
\rho &= \rho_{\text{Brocher}}\left(v_s - \frac{\partial v_s}{\partial T}\Delta T\right) + \frac{\partial \rho}{\partial T}\Delta T \\
&= \rho_{\text{Brocher}}\left(v_s - \frac{v_S}{v_P}\frac{\partial v_p}{\partial T}\Delta T\right)\left(1-\alpha\Delta T\right) \\
&= \rho_{\text{Brocher}}\left(v_s + 0.28\frac{\text{m/s}}{°\text{C}}\Delta T\right)\left(1-2.5\cdot 10^{-5}(°\text{C})^{-1}\Delta T\right)
\end{aligned} \tag{4}$$

where $r_{\text{Brocher}}(v_s)$ is the combined regression of v_s on v_p and v_p on density of Brocher.

For example, a 0.1 km/s increase in velocity due to compositional variations would predict a ~54.5 kg/m^3 higher density, but if this 0.1 km/s increase was because this crust (reference density 2750 kg/m^3) was colder than our reference by 356°C, the density would only increase ~24.9 kg/m^3. We overestimate density of "warm" material by a factor of ~0.08 kg/m^3 °C^{-1}. Thus modest velocity variations due to temperature can lead to tectonically significant errors in predicted density (in a 40 km crust, the error above would produce ~400 meters of topography), and ascribing all velocity heterogeneity to composition or to temperature will lead us to calculate inaccurate densities.

Taking these inferred temperature perturbations (Figure 4d) into account, we calculate crustal topography throughout the western U.S. (Figure 4b). We note that *S*-wavespeed variations caused by melt (7.9% decrease per 1% in situ melt fraction) produce far smaller changes in bulk density than composition or temperature (between 0 and 4 kg/m^3 per 1% in situ melt fraction)[*Hammond and Humphreys*, 2000]. This bias will cause H_c

as calculated here to be too great in areas with crustal melts. Areas of topographic misfit are addressed explicitly below.

4. Topography Uncertainties

The posterior distribution of wavespeed structures from the Monte-Carlo investigation of seismic models of Shen et al. (2013b) allows for a direct analysis of the uncertainty of our topographic calculations due to seismic uncertainties. Each individual velocity profile and crustal thickness is converted into a density profile, and the attendant crustal and mantle topographies are calculated. The resulting ~1000 estimates of H_c and H_m at each point define the seismic uncertainty in our results (Figure 4f).

We have quantified the uncertainty in our topography estimates and investigated its origins. We find that the variation in elements of the posterior distribution of v_s models overwhelms the uncertainties in converting velocity to density. As illustrated in Figure 2, basing predictions of elevation on a single velocity profile not only may produce systematically biased results but also underestimates the uncertainty of the prediction, even if the uncertainty in density derived from velocity is considered. In fact, once the full posterior distribution of velocity models is analyzed, incorporation of such uncertainty yields no further variation in the predicted topography. Even if deviations from the presumed velocity-density relationship correlate over layers 10 km thick, uncertainties in H_c rise by less than 50 meters. Vertical correlations would have to be crustal in scale, significantly greater than the ~5 km length suggested by investigations of the Ivrea Zone [e.g., *Goff et al.*, 1994; *Levander and Holliger*, 1992; *Holliger and Levander*, 1992], to have an impact comparable to the uncertainty in velocity profiles. Thus, we do not include uncertainties in the velocity to density conversion in our uncertainty of H_c. Substantial and systematic deviations of a region from the assumed velocity-density relationship will produce equally systematic deviations of the calculated topography from that observed. We discuss such occurrences below.

As noted above, the negative covariance between crustal velocities (and thus H_c) and mantle velocities (and thus H_m) reduces uncertainty in overall estimated topography (Figure 4f) somewhat from that expected from the two components. Standard deviations of estimates of H_c, H_m, and calculated elevation (e_c) at each of the stations have means of 161 meters, 270 meters, and 306 meters, respectively.

A potential difficulty arises if large magnitude, long wavelength variations in radial anisotropy are present. We have assumed that the v_{SV} profiles used are sufficiently close to the mean shear wave speed of the crust and mantle for calculation of densities. However, the presence of variations in radial anisotropy would produce biases: we would be underestimating the Voigt average shear velocity by ~1.5% in areas where radial anisotropy was ~5% , in which case we would overpredict topography by about 800m relative to isotropic sections if the anisotropy extended through the entire crust and mantle to ~150 km depth. Variations inferred by Moschetti et al. [2010] for the area west of 110°W suggest we might be underpredicting elevation in the Colorado Plateau and further underpredicting elevation in the Sierra Nevada by some few hundred meters. At a longer wavelength, the model of Marone et al. [2007] suggests that we could be overpredicting elevations in the southern Rockies by several hundred meters. Owing to the present low-resolution and lateral variability of models of radial anisotropy, we do not explicitly correct for this effect.

Other limitations that could affect our results arise from the parameterization of the seismological model. Crustal low-velocity zones are prohibited, and sharp increases in wavespeed are only permitted at the base of sediments and at the Moho. The presence of crustal low-velocity zones is probably limited in extent; depending on the exact mismatch, presumably the mean crustal velocity is approximately maintained and little or no error will be introduced into our calculations. Strong discontinuities at depth other than the Moho could result in material being assigned the wrong velocity to density function; this is presumably most likely in areas where "double Mohos" are present (e.g., southern Wyoming [*Karlstrom et al.*, 2005]). The error here depends on whether the seismic inversion has selected the top or bottom Moho and the velocity of the material between the two Mohos. Errors from this limitation are likely to be under 300m for a 10 km thick layer misplaced above or below the Moho.

5. Comparison to Topography and Adjustments to Densities

Where our combined crustal (Figure 4b) and mantle (Figure 4a) variations reproduce observed topography acceptably (to the limits shown in Figure 4h), lithospheric thermal and crustal compositional variations are sufficient to support the topography. Elsewhere, other factors presumably affect the velocity-density relationship or the surface elevation such as crustal melt, compositional variations in the mantle, lithospheric mantle extending below the model, or normal stress derived from the convective regime of the asthenosphere (dynamic topography). To identify these areas more clearly, we calculate the residual topography, H_r, (Figure 4g) which represents the smoothed topography (Figure 1a) minus the topography calculated from our initial assumptions, e_c.

$$H_r \equiv \varepsilon - e_c = \varepsilon + H_0 - H_c - H_m \tag{5}$$

Thus, positive residual topography denotes a higher observed elevation than predicted by a given model. In light of the appreciable uncertainties (mean 2σ=590 meters), we pay particular attention to regions where H_r exceeds our calculated uncertainty (Figure 5a).

As seen in Figure 5a, elevations in ~84% of the study area are matched within uncertainty by a combination of compositional and thermal variations in the crust and thermal variations in the mantle. In the Yellowstone region, Cascadian forearc, and Southern Rocky Mountains, elevations are coherently predicted to be 0.5-1 km higher than observed. This discrepancy can be eliminated by imposing a downward normal stress of 15-30 MPa on the lithosphere (i.e., dynamic subsidence), or systematically increasing lithospheric density, which is plausibly accomplished by correcting for melt in the crust or mantle.

Near Yellowstone and in the southern Rockies, negative residual topography coincides with heat flow in excess of 100 mW/m^2 (Figure 4c), high seismic attenuation in the crust [e.g., *Phillips and Stead*, 2008] and inferred near- or supra-solidus mantle temperatures (see Figure 4a). We thus propose that partial melt is present in the crust in these areas (Figure 5b), though we recognize that presence of melts in the mantle at sub-solidus temperatures would also produce an error in calculated density. In a crustal column with original *S*-velocity of 3.15 km/s that contains an average 1% melt, wavespeeds decrease by 0.25 km/s [following *Hammond and Humphreys*, 2000]. We would misinterpret such a decrease as a 147 kg/m^3 density decrease, and, when integrating through a 40 km crustal column, would overestimate crustal topography by 1.85 km. Thus, ~0.6% in situ partial melt throughout the ~40 km crust near Yellowstone would account for 1 km residual topography, as would 6% in a 4 km zone; we do not aim to discriminate between distributed and concentrated crustal melt especially as the shear wave structures we use prohibit crustal low velocity zones. An identical average amount of melt would resolve the discrepancy in the southern Rockies, though this could be lessened if radial anisotropy is indeed stronger in this area.

Conversely, -0.5 to -1 km residual topography in the Cascadian forearc coincides with low heat flow. Geologically, the presence of substantial amounts of serpentine, with its unusual wavespeed to density relationship, might be expected to contribute to this error. Although serpentinization lowers v_s substantially, using the regressions of Brocher (2005) of v_s to v_p and v_p to density produces a misfit of only 111 kg/m^3. A 10 km layer that is 50% serpentine increases estimated topography by only 175 meters. We thus propose that the forearc is depressed by downward basal normal stresses of ~15-30 MPa exerted on the lithosphere by subduction zone processes (Figure 5d).

Elevations in the southern Sierra Nevada and northern Basin and Range (Figure 5a) and to a lesser extent Wyoming and the Idaho batholith (Figure 4g) are higher than expected by as much as 500 meters. Overestimating density by 40 kg/m^3 throughout a 40 km crust would account for this discrepancy. We suspect that particularly felsic crust, and its attendant low v_p/v_s leads us to calculate systematically high densities, since we use Brocher's regressions of v_s onto v_p and v_p onto density. To estimate the mean amount of quartz increase necessary to reconcile seismic velocities and topography, we compare the observed and predicted densities of pure quartzite [*Christensen*, 1996], assuming that the polynomial regression [*Brocher*, 2005] is appropriate for average continental crust of ~60% SiO_2 containing ~10% quartz. The density estimated from our application of Brocher's regressions for a v_s of 4.035 km/s (200 MPa quartzite) is 2975 kg/m^3, but the density of quartzite is only 2652 kg/m^3. Thus an increase in the modal abundance of quartz of ~90% corresponds to a 325 kg/m^3 bias in density. Thus, a 500 meter elevation error can be explained by an increase in the modal abundance of quartz of ~11% throughout the crust. These regions (Figure 5c) coincide with low v_p/v_s estimated from receiver functions that Lowry and Perez-Gussinye [2011] interpret as reflecting a high quartz content.

Overestimated topography could also be attributed to variations in mantle chemistry. Increasing Mg# (Mg#=MgO/[MgO+FeO]) of olivine in mantle lithosphere both increases velocity (~0.3% per 0.01 increase in Mg#) and decreases density (~8.5 kg/m^3 per unit increase in olivine Mg#) [*Schutt and Lesher*, 2010]. Thus, an increase of ~0.01 in Mg# can resolve the apparent discrepancy between seismic velocity and elevation. Because the only province where we might suspect significant iron depletion and we observe large magnitude, large wavelength,, positive residual topography is the Wyoming craton (Figure 5a), we do not investigate this mechanism further here.

To account for the effects of melt and varying quartz content, we thus propose to modify the density structures calculated assuming thermal variations throughout the lithosphere and compositional variations in the crust (topography of which is shown in Figure 4). These modifications affect ~16% of the study area. To recover topography, a mean crustal density adjustment of Δρ

$$\Delta\rho = -H_r\left(\frac{\rho_a}{z_c}\right) \qquad (6)$$

is necessary, with residual topography, H_r, as defined in eqn. 5, asthenosphere density ρ_a=3200 kg/m^3, and crustal thickness z_c. Adding this term to the previously derived structures yields an adjusted density structure and an adjusted crustal topography (Figure 6d).

These adjustments are relatively small, especially when compared to the ~60 kg/m^3 standard errors associated with a linear velocity-density scaling [*Christensen and Mooney*, 1995]. Where applied, the mean increase in crustal density due to melt is 23.5 kg/m^3, and the mean decrease in crustal density from quartz content is -17.7 kg/m^3.

6. Results

With the adjusted density estimates as described above, we examine three characteristics: the decomposed topography, predicted gravity, and gravitational potential energy.

6.1 Topography

We have determined a set of mantle and crustal densities that accord with both seismic velocity and topography. Nearly all of the variation in topography (Figure 1a, 6a) across the western U.S. arises from compositional (Figure 6c,f) and thermal (Figure 6b,e,h) variations expressed in wavespeed variations. Elsewhere (Figure 5a), in areas where crustal melt or highly felsic crust [*Lowry and Perez-Gussinye*, 2011] are likely, the relationship between velocity and density must be adjusted. Taking these adjustments (eqn. 6) into account, we can further separate modern topography into thermal and compositional components (Figures 6-7).

There are exactly four topographic components other than dynamic topography (Figure 5d, 6i): mantle thermal (Figure 6h), mantle compositional, crustal thermal (Figure 6e), and crustal compositional (Figure 6f; where both thickness (Figure 1b) and chemistry (Figure 8) are considered) . We have assumed that all density and velocity variations in the mantle are thermal in origin and have found no locations violating this assumption (at least above 150 km depth). In the crust, we have estimated a mean temperature and thus (following eqn. 2) the effect of thermal expansion (Figure 6e) and contraction, Hc_{thermal}, is:

$$Hc_{\mathrm{thermal}} = z_c \rho_0 \, \alpha \, \Delta T/\rho_a \qquad (7)$$

where z_c is crustal thickness, ρ_0 is the crustal density α is the coefficient of thermal expansion (2.5×10^{-5} °C^{-1}), and ΔT is derived from heat flow. Then, the crustal compositional topography (Figure 6f) is given as:

$$Hc_{\mathrm{comp}}=H_c-Hc_{\mathrm{thermal}} \qquad (8)$$

Examining the different components of topographic support (Figures 6-7), it is clear that differences in elevation among the southern Basin and Range, the Great Basin, the Colorado Plateau and the southern Rockies are mostly to be found in differing crustal characteristics (Figure 6d-f) rather than heterogeneity in the mantle.

Wyoming, the one Cordilleran province lacking warm mantle, is higher than the plains because of higher crustal compositional topography (Figure 6f). We note also that since our density models recover topography and gravity (presented below) in the Wyoming craton reasonably well, the high velocities observed below 150 km [e.g., *Burdick et al.*, 2008] either represent cold but iron-poor isopycnic material or require somewhat lower densities in the mantle above 150 km.

Mantle topography accounts for the eastward descent from 2.5 km elevations in the Rockies to less than 1 km in the Great Plains.

6.2 Comparison to Gravity

Our adjusted density structure can be tested by calculating gravity anomalies from it and comparing these to the observed Bouguer anomaly (an alternative approach, as followed by Mooney and Kaban [2010], uses gravity as a primary observable and deduces density variations from gravity). We note first, however, that the predicted gravity field at a given station is strongly dependent on the shallow structure beneath that station. The top few km is poorly constrained seismically because of limited sampling at higher frequencies. Furthermore, the use of receiver functions in determining acceptable seismic models can impart a local bias; the structure beneath a station may not be representative of the surrounding ~70 km. From our 2s uncertainty on predicted topography of ~600m, we would expect to recover the Bouguer gravity anomaly only to within ~65 mGal.

We estimate the Bouguer anomaly from our preferred 3D density, including adjustments for inferred crustal melt and quartz enrichment; details are presented in the appendix. The 3D gravity prediction (Figure 9a) recovers the overall Bouguer anomaly variations of the western U.S. (Figure 9b) within expectations (Figure 9c). The misfit has mean magnitude of 25 mGal, near a crude estimate of uncertainty, discussed in the appendix. The misfit is less than 60 mGal in 95% of the study area and below 30 mGal in 75%, about what we would expect from the uncertainty in predicted topography.

6.3 Gravitational Potential Energy

Lateral variations in pressure that arise from density differences generate stresses within the lithosphere, with areas of high integrated pressure (or GPE) exerting compressive stress on adjacent regions of lower GPE. From distributions of density, we can calculate body forces available to modulate the stress field imposed by basal and edge forces.

$$GPE = \int_{0}^{150+E} \rho(z) g z \, dz \qquad (9)$$

where z is positive upward from the model base (in this case 150 km depth, such that mean sea level is at z=150 km), and$E$ is the surface elevation. We compare GPE to that of an asthenospheric column [*Jones et al.*, 1996] of density 3200 kg/m^3 that extends from 150 km to 2.4 km depth (order 10^{14} N/m). This column is calculated to be in isostatic equilibrium with a mid-ocean ridge [*Lachenbruch and Morgan*, 1990]. Such a column of asthenosphere should be free of deviatoric stresses, making it a useful reference state. High potential energy (positive anomaly, ΔGPE, relative to an asthenospheric column) increases horizontal deviatoric extensional stresses while negative ΔGPE favors contractional deformation. Lateral variations in ΔGPE are of the order 10^{12} N/m (Figure 10), and uncertainties are of the order 10^{11} N/m, up to 10^{12} N/m.

The mean deviatoric stress exerted by one idealized column on another is the difference in GPE divided by the column, or lithospheric, thickness [e.g., *Sonder and Jones*, 1999]. To illustrate, for two adjacent 200 km columns with a GPE contrast of 2 x 10^{12} N/m, the mean deviatoric stress exerted is 10 MPa. The magnitudes of these stresses are used by geodynamicists to calculate the magnitude of plate boundary stresses in the continental interior and to estimate the bulk viscosity of the lithosphere in thin viscous sheet models [e.g., *Flesch et al.*, 2007].

Positive ΔGPE is most prominent in the Sierra Nevada and the northern Basin and Range. The eastern front of the Sierra is, in fact, a locus of modern extension (e.g., Unruh and Hauksson, 2009) and the northern Basin and Range has been previously suspected to be a region of highly positive GPE [*Humphreys and Coblentz*, 2007; *Jones et al.*, 1996]. The large-scale negative ΔGPE along the western margin of North America may be the result of surface depression due to subduction related dynamic pressures (especially north of the Mendocino Triple Junction). A limb of negative ΔGPE projects eastward from the Cascade margin at ~46 °N. This anomaly coincides with the Yakima Fold and Thrust Belt, a zone of Quaternary deformation that may be connected to compressional strain along the Cascade margin [*Blakely et al.*, 2011]. We propose that body forces modulate edge and basal stresses to create this pattern of contractional deformation.

7. Discussion

7.1 Topography and earlier studies

The explanation of western US topography presented here differs from that inferred in earlier work; we consider here the origins of those differences and the implications for the validity of our results. Jones et al. (1996) did not use any seismological information for the mantle and instead inferred variations in H_m by assuming isostatic compensation in the asthenosphere. Values of H_c were mainly derived from *P*-wave refraction profiles using the Christensen and Mooney (1995) wavespeed-density regressions with no correction for lateral thermal variations. Most of our values of H_c are quite similar where seismic models were available to Jones et al.; the most notable differences are significantly lower H_c values (Figure 6d) in the California Central Valley and Colorado High Plains (which are due at least in part to the thermal effects on crustal wavespeed-density relations that Jones et al. ignored) and somewhat lower values in the northern Basin and Range. We only find ~350 m variation in support from the mantle within the Cordillera outside Wyoming (Figure 6f), about one quarter that of Jones et al. (1996). The differences mainly reflect the explicit inclusion of mantle wavespeed anomalies here and suggests that most of the topography Jones et al. attributed to mantle density variations is caused by other effects.

Hasterok and Chapman [2007b] focused on a more complex thermal analysis of North America but overall used nearly identical assumptions as Jones et al in correcting for varying compositional H_c in trying to reproduce topography across the region. We limit the use of surface heat flow to estimate crustal temperatures but Hasterok and Chapman (2007b) extended this use into the mantle. Although we share an assumption of a thermal origin for mantle density anomalies, we rely on seismic wavespeeds to estimate mantle temperatures and thus density. Furthermore, we adjust observed wavespeeds to account for thermal variations before interpreting chemical variations in the crust. They estimated, as we do (compare their Figure 4c with our Figure 6b), that thermal variations account for ~3 km of relief. The differences between surface heat flow and seismic wavespeeds at depth suggests that much of the scatter Hasterok and Chapman found can be attributed to non-steady-state thermal structure within the lithosphere. Unlike an extrapolation of surface observations into the mantle, our approach permits different thermal structures in the crust and mantle, implicitly allowing non-steady state geotherms, which are reflected by seemingly inconsistent crustal (Figure 6d) and mantle (Figure 6g) thermal topography as in the Sierra Nevada and Colorado Plateau.

Our estimates of crustal compositional topography (Figure 6c) variations are generally of the same polarity but of different magnitude from Hasterok and Chapman's (2007a). Specifically, we tend to calculate much greater variations of crustal buoyancy within the Cordillera. For example, comparing the northern and southern Basin and Range, we propose that nearly all of the ~1 km of relief is compositional in origin, as are differences between these provinces and the southern Rockies (Figure 6c). In each case, Hasterok and Chapman [2007b] ascribe this relief to thermal variations.

Lowry et al. (2000) inferred from an analysis considering gravity and some seismic refraction models that about 2 km of topographic variation was caused by dynamic stresses applied to the lithosphere. Although our crustal buoyancy estimates are fairly close to theirs (compare our Figure 6d and their Plate 3b), we have a very different appraisal of the topography due to thermal effects in the mantle largely because we are interpreting seismic models in the mantle, but they projected surface heat flow measurements into the mantle. This disparity suggests that the lithosphere in the region is either not in a conductive steady-state or has large deviations in conductivity or heat production from values presumed by Lowry et al., and this difference is why we do not infer the significant dynamical component to topography that they reported away from the subduction zone.

7.2 Examples of application to province-scale tectonics

One can interrogate this subcontinental-scale model of the sources of topography to examine province-scale tectonics in a regional context. The comparison of two provinces, for example, allows for an explanation of modern relief. As an example, we explore the topographic disparity of the southern and northern Basin and Range (Figure 1a, 6a). The comparison of modern elevations in one province to an estimated paleoelevation and examination of the modern topographic components constrains the changes that may be responsible for surface uplift or subsidence. We illustrate such a use in the Colorado Plateau.

The ~800 meters of relief between the southern and northern Basin and Range has been variously attributed to plume-derived dynamic topography [*Saltus and Thompson*, 1995], variations in mantle lithospheric thickness [*Jones et al.*, 1996] and/or chemistry [*Schulte-Pelkum et al.*, 2011] and variations in crustal density [*Eaton et al.*, 1978]. Examining Figures 6-8, we conclude that relief is generated by crustal compositional variation, not by mantle variations. Furthermore, this elevation difference is due not to crustal chemistry; mean thermally-corrected densities (Figure 8) are 2726 kg/m^3 in the southern and 2716 kg/m^3 in the northern Basin and Range, which contributes ~100 meters of relief. Instead topography arises from a crustal thickness difference of 4.5 km (Figure 1b), which accounts for 700 meters of relief. Note that this interpretation is at odds with earlier estimates based on refraction studies [e.g., *Catchings and Mooney*, 1991] that showed a ~30 km crustal thickness throughout the Basin and Range. The receiver functions used here and other continent-scale receiver function studies [e.g., *Gilbert*, 2012] allow for a more uniform sampling of crustal thickness whereas refraction lines may preferentially sample anomalously thin or thick crust in a given region.

The Colorado Plateau has risen ~2 km since the Cretaceous, and this uplift has been attributed to 1) warming of the uppermost mantle either conductively [*Roy et al.*, 2009] or by removal of the lower lithosphere recently [*Levander et al.*, 2011] or during the Laramide (Spencer, 1996), 2) dynamic support from the mantle convective regime [*Moucha et al.*, 2008], or 3) crustal thickening due to lower crustal flow (McQuarrie and Chase, 2000) or a lower crustal phase change [*Morgan*, 2003; *Jones et al.*, 2011]. We find that the mantle thermal topography (compare Colorado Plateau and Great Plains in Figure 8) and the crustal chemistry (compare Colorado Plateau to southern Rockies in Figure 8) are responsible for the modern elevation (compare Colorado Plateau to southern Rockies in Figure 8), and modern topography does not require dynamic support. The 30 kg/m^3 difference in crustal chemical density between the Rockies and Colorado Plateau that we estimate lends ~500 meters of relative support to the latter. Hydration of lower crust, as recorded in xenoliths [e.g., *Butcher*, 2013] is one possible means of changing crustal density since the Cretaceous. The remaining 1.5 km of uplift is suspiciously similar to the difference in mantle thermal topography between the Colorado Plateau and the lower part of the Great Plains (Figure 6h). If the continental interior serves as an estimate for the pre-Cretaceous Colorado Plateau [*Spencer*, 1996], then a change in the mantle thermal structure largely explains the change in topography. The magnitude of this inferred change suggests that mechanical replacement of the lower thermal boundary layer is more likely than conductive heating. For a ~90 km thick lithosphere [e.g., *Levander and Miller*, 2012] and 40 km thick crust, the <u>mean</u> mantle lithospheric temperature would have to change by ~940 °C (and thus the base of the lithosphere by nearly 2000 °C , even in the endmember case of a linear geotherm) to produce 1.5 km of uplift, whereas removal of 85-110 km of thermally equilibrated mantle lithosphere (i.e., with a linear geotherm) would produce 1.5 km of uplift [*Levandowski et al.*, *in preparation*].

7.3 Implications for dynamic topography

Previous workers have invoked dynamic topography, or basal normal forces exerted by the convective regime of the asthenosphere, to explain elevations of the Colorado Plateau [*Moucha et al.*, 2008], the southern Rockies [*Karlstrom et al.*, 2012] or Yellowstone [e.g., *Pysklywec and Mitrovica*, 1997]. Nevertheless, we present densities that recover modern elevations reasonably well, and since the gravity misfit (Figure 9c) is within expectations of our topographic uncertainties, we largely reject the role of dynamic pressures in supporting topographic variations in the Cordillera, except east of the vicinity of the Cascadia subduction zone (Figure 5d).

To illustrate, consider a region at sea level with isopycnic mantle lithosphere (i.e., H_m=0) and 40 km thick crust of uniform density. If in isostatic equilibrium (i.e., H_c=2.4 km), the crust must be 3008 kg/m^3. If a ~1 km of dynamic topography (basal normal force of ~30 MPa) is being generated by asthenospheric convection (i.e., H_c=1.4 km), then crustal density is 3088 kg/m^3. The difference in the gravity signal from these two crustal columns is ~135 mGal in the infinite slab limit and 118 mGal if active over 300 km wavelength. Thus, given the absence of large magnitude, province-scale gravity residuals, we argue that the density structure that we estimate, and not dynamic topography, is responsible for the modern elevation of the western U.S..

7.4 GPE and earlier studies

Previous attempts to estimate GPE have relied upon the filtered geoid or interpolations of seismic models. Our work improves upon shortcomings of the former by including long-wavelength variations due to shallow (<150 km) structure and upon the latter by utilizing a near-uniform model coverage and uniform seismic data processing methods.

The locations of relative GPE anomalies vary substantially in earlier studies. In a study of similar spatial dimensions to ours, Flesch et al. (2007) estimate a GPE high in the southern Rocky Mountains and a general gradient downward toward the Pacific margin. Using the geoid somewhat differently, Humphreys and Coblentz (2007) suggested that the northern Basin and Range broadly, and northeastern Nevada specifically, was a region of high GPE and that the Rockies were nearly without GPE-derived deviatoric stresses. Jones et al. (1996) also found high GPE in northeastern Nevada, when using seismic velocities instead of the geoid. But unlike later work, they also found high GPE in the Sierra Nevada, low GPE on the western margin, and variable GPE in the southern Rockies. Our work, perhaps not surprisingly, more closely resembles this previous effort that uses seismic velocity than those using geoid. We find GPE highs in NE Nevada and the Sierra Nevada and a coherent, consistent GPE low along the western margin of the continent (Figure 10).

The magnitudes of GPE anomalies are comparable to previous estimates [*Jones et al.*, 1996; *Flesch et al.*, 2007; *Humphreys and Coblentz*, 2007]. Ranges have been estimated at 4.5 TN/m, 9 TN/m, and 4.5 TN/m, respective to the citations above. Our estimated range is ~7 TN/m (with the exception of the unreliable edges of our model).

Although the full impact of our new GPE estimates requires a more complete analysis, certain effects can be illustrated by simple analogy. If using modeling strain rates (e.g., Flesch et al., 2000), higher strain rates require higher deviatoric stresses (which can be from higher ΔGPE) or lower average viscosity. To a certain degree, areas with higher GPE than used before will need a higher viscosity to match observed strain rates. Thus in areas such as the southern Rockies, where our estimated ΔGPE is lower than Flesch et al. (2000), the viscosity estimated would be lower, and in areas such as the eastern Sierra and parts of the Basin and Range where our estimate of GPE is higher, the viscosity would also be higher. In other approaches (e.g., Flesch et al., 2007) where stresses (or strain rate orientations) are fit, the variation in magnitude of GPE affects the orientation of the stress field (e.g., contrast Figs. 4a and 4c of Flesch et al., 2007) which in turn effects the plate boundary stresses needed to recover modern stresses or strain rate orientations.

8. **Conclusions**

We have generated a density model of the western U.S. lithosphere from surface heat flow and seismic models at the well-distributed Transportable Array stations and quantitatively checked it against predicted topography and gravity. Large overestimates of elevation (>600m) near Yellowstone and in the southern Rocky Mountains are attributed to the presence of lithospheric melt, while we attribute some underestimates of topography to anomalously quartz-rich crust. Overestimated elevations near the Cascadia subduction zone probably are caused by dynamic effects up to ~1 km. Correcting for these effects yields our final density structure.

The origin of topographic variations within the western U.S. can be examined by decomposing the elevation field into its five components: crustal thermal, mantle thermal, crustal compositional, mantle compositional and dynamic topography (Figure 6). Crustal composition (Figure 6f) and mantle temperatures (Figure 6h) dominate both in magnitude and heterogeneity. Dynamic topography (Figure 6i) is only locally important along the plate boundary, whereas crustal thermal topography (Figure 6e) is of low magnitude across the region. We find no statistically significant need for elevation variations derived from mantle composition, though variations of several hundred meters are possible.

The Cordillera overlies nearly constant-density mantle (Figures 6g, 6h), and topographic relief generally reflects variations in crustal thickness and chemistry. One exception is the relief between the Colorado Plateau and southern Rockies, which is due in large part to crustal temperature differences (>500 m of ~1 km; Figure 6g).

The Wyoming craton overlies cold, dense mantle (Figure 6h), but thick crust (Figure 1b) allows modest elevations. High velocities observed below 150 km [e.g., *Burdick et al.*, 2008] presumably record cold mantle that is either itself isopycnic with surrounding asthenosphere or requires the mantle lithosphere above 150 km to be depleted and less dense than we infer here. Elevation decreases eastward into the Great Plains are due to chemically denser crust (Figure 8).

Away from the Cascadia subduction zone, our results limit topographic effects of dynamic stresses to under a few hundred meters. Our seismologically based density structure reproduces elevations within 600m at the 2s level. Significant dynamic effects should produce large errors in our predicted gravity field, but the differences between observed and predicted gravity are as expected from seismologically derived uncertainties.

Finally, we have uniformly quantified the variations in gravitational potential energy throughout the western U.S. (Figure 10). Positive GPE anomalies favor horizontal extension in the Northern Basin and Range and along the eastern front of the Sierra Nevada. Compression in the Yakima fold and thrust belt, conversely, coincides with negative anomalies.

Acknowledgments

Early efforts on this work were funded by NSF grant EAR-060783 and seismic model construction was supported by NSF grant EAR-10543291. We thank Peter Molnar for an insightful review.

Appendix

We use our preferred 3-D density model—with adjustments for inferred melt and magnesium enrichment included—to calculate the Bouguer gravity anomaly. This model has nodes every 1 km in depth to 15 km below sea level, every 5 km from 15 to 50 km depth and every 10 km to 150 km depth. We interpolate the density estimates at all stations to a uniform grid with 65 km horizontal spacing. To broadly mitigate edge effects and computational artifacts, we subtract a reference structure of 2670 kg/m^3 from the station elevation to sea level (effectively reproducing the Bouguer correction), 2800 kg/m^3 from the surface to 40 km depth and 3200 kg/m^3 below that. The density structure is then represented by rectangular prisms 65 x 65 km in plan view and as thick as the node spacing at each depth.

To further limit edge effects we must consider the physiography and geology of surrounding regions. We place 50 km thick crust within the mountains north (Canadian Rockies) and south (Mexican Rockies) of our model (represented by prisms of +118 kg/m^3 between 0 and 40 km and -281 kg/m^3 between 40 and 50 km depth) over our reference mantle. East of the Canadian Rockies, where elevations are ~500 meters we use a 40 km crust over reference mantle (prism of +118 kg/m^3 between 0 and 40 km). No adjustment is made to the east as our model extends >300 km east of 102°W, well beyond what we show here. At the Cascadia subduction zone, we approximated the upper portion of the Juan de Fuca slab (beyond the western boundary of the seismic models) as a tabular body with a density perturbation of +200 kg/m^3, thickness of 40 km, dip of 35° and depth of 75 km at the western edge of the study area. This body produces a signal of ~+150 mGal at its western edge that decreases eastward by roughly 30 mGal per 100 km. Southward along the coast, we approximate the Pacific Plate as a 10 km thick, 3000 kg/m^3 crust (+200 kg/m^3 1-11 km) underlain by 3200 kg/m^3 mantle (+400 kg/m^3 11-40 km) and overlain by 1 km of sea water (-1800 kg/m^3 0-1 km). This body produces a ~200 mGal anomaly that decays quickly (<100 mGal within 100 km of the coast).

Gravity is calculated by summing the contributions at each grid point from all of the prisms below the station within the model. To compare with observed gravity, we add a static term--the average of Bouguer anomaly observations-- to our predicted Bouguer gravity anomalies.

The contribution to errors in our calculated gravity from seismological uncertainty may be estimated by calculating the predicted 1-D gravity anomaly for each of ~1000 acceptable velocity profiles at each station. Uncertainties for 1D gravity predictions vary from ~+/-10 mGal to ~+/-40 mGal (2σ). Uncertainties for our 3-D gravity will be less to the degree that errors in seismic wavespeeds are not correlated with distance.

References

Bird, P. (1988), Formation of the Rocky Mountains, western United States: A continuum computer model, *Science*, *239*, 1501-1507.

Blakely, R. J., B. L. Sherrod, C. S. Weaver, R. E. Wells, A. C. Rohay, E. A. Barnett, and N. E. Knepprath (2011), Connecting the Yakima fold and thrust belt to active faults in the Puget Lowland, Washington, *JGR*, *116* (B7), DOI: 10.1029/2010JB008091.

Brocher, T. (2005), Empirical relations between elastic wavespeeds and density in the Earth's crust, *Bulletin of the Seismological Society of America*, *95* (6), 2081-2092, DOI: 10.1785/0120050077.

Burdick, S., C. Li, V. Martynov, T. Cox, J. Eakins, T. Mulder, F. Vernon, G. Pavlis, and R. D. van der Hilst (2008), Upper Mantle Heterogeneity beneath North America from Travel Time Tomography with Global and USArray Transportable Array Data, *Seismological Research Letters*, *79* (3), DOI: 10.1785/gssrl.79.3.384.

Butcher, L. (2013), Re-thinking the Laramide: Investigating the Role of Fluids in Producing Surface Uplift Using Xenolith Mineralogy and Geochronology, M.S. thesis, 79 pp, University of Colorado.

Catchings, R. D., and W. D. Mooney (1991), Basin and Range crustal and upper mantle strucutre, northwest to central Nevada, *Journal of Geophysical Research*, *96* (B4), 6247-6267.

Christensen, N. I. (1996), Poisson's ratio and crustal seismology, *Journal of Geophysical Research*, *101* (B2), 3139-3156.

Christensen, N. I., and W. D. Mooney (1995), Seismic velocity structure and composition of the continental crust: A global view, *J. Geophys. Res.*, *100* (B7), 9761-9788.

Ducea, M. N., and J. B. Saleeby (1996), Buoyancy sources for a large, unrooted mountain range, the Sierra Nevada, California: Evidence from xenolith thermobarometry, *Journal of Geophysical Research*, *101* (B4), 8229-8244.

Eaton, G. P. (1986), A tectonic redefinition of the Southern Rocky Mountains, *Tectonophysics*, *132* (1-3), 163-193.
Eaton, G. P., R. R. Wahl, H. J. Prostka, D. R. Mabey, and M. D. Kleinkopf (1978), Regional gravity and tectonic patterns: Their relation to late Cenozoic epeirogeny and lateral spreading in the western Cordillera, in *Cenozoic Tectonics and Regional Geophysics of the Western Cordillera*, edited by R. B. Smith and G. P. Eaton, pp. 51-91, Geol. Soc. Am., Boulder, Colo.
Flesch, L. M., W. Holt, A. J. Haines, and B. M. Shen-Tu (2000), Dynamics of the Pacific-North American plate boundary in the western United States, *Science*, *287* (5454), 834-836, DOI: 10.1126/science.287.5454.834.
Flesch, L. M., W. Holt, A. J. Haines, L. X. Wen, and B. M. Shen-Tu (2007), The dynamics of western North America: stress magnitudes and the relative role of gravitational potential energy, plate interaction at the boundary and basal tractions, *Geophys J. Int.*, *169* (3), 866-896, DOI: 10.1111/j.1365-246X.2007.03274.x.
Flesch, L. M., and C. Kreemer (2010), Gravitational potential energy and regional stress and strain rate fields for continental plateaus: Examples from the central Andes and Colorado Plateau, *Tectonophysics*, *482*, DOI: 10.106/j.tecto.2009.07.014.
Gilbert, H. (2012), Crustal structure and signatures of recent tectonism as influenced by ancient terranes in the western United States, *Geosphere*, *8* (1), DOI: 10.1130/GES00720.1.
Goff, J. A., K. Holliger, and A. Levander (1994), Modal fields: A new method for characterization of random seismic velocity heterogeneity, *GRL*, *21*.
Grand, S. P., and D. V. Helmberger (1984), Upper mantle shear structure of North America, *Royal Astronomical Society Geophysical Journal*, *76*, 399-438.
Hacker, B. R., and G. A. Abers (2004), Subduction Factory 3: An Excel worksheet and macro for calculating the densities, seismic wave speeds, and H2O contents of minerals and rocks at pressure and temperature, *Geochem Geophy Geosy*, *5*, -, DOI: 10.1029/2003GC000614
Hammond, W. C., and E. Humphreys (2000), Upper mantle seismic velocity: Effects of realistic partial melt geometries, *JGR*, *105* (B5), 10975-10986.
Hasterok, D. P., and D. S. Chapman (2007a), Continental thermal isostasy: 1. Methods and sensitivity, *JGR*, *112* (B06414), DOI: 10.1029/2006JB004663.
Hasterok, D. P., and D. S. Chapman (2007b), Continental thermal isostasy: 2. Application to North America, *JGR*, *112* (B06415), DOI: 10.1029/2006JB004664.
Haxby, W. F., and D. L. Turcotte (1978), On isostatic geoid anomalies, *JGR*, *83* (B11).
Holbrook, W. S. (1990), The crustal structure of the northwestern Basin and Range Province, Nevada, from wide-angle seismic data, *Journal of Geophysical Research*, *95* (13), 21,843-821,869.
Holliger, K., and A. Levander (1992), A stochastic view of the lower crust based on the Ivrea Zone, *GRL*, *19* (11).
Humphreys, E. (2009), Relation of Flat Subduction to Magmatism and Deformation in the Western USA, *GSA Memoir*, *204*, DOI: 10.1130/2009.1204(04).

Humphreys, E., and D. Coblentz (2007), North American dynamics and Western US tectonics, *Rev. Geophys.*, *45* (RG3001), DOI: 10.1029/2005RG000181.

Jackson, I., and U. H. Faul (2010), Grainsize-sensitive viscoelastic relaxation in olivine: Towards a robust laboratory-based model for seismological application, *Phys. Earth Planet. Inter.*, *183*, 151-163, DOI: 10.1016/j.pepi.2010.09.005.

Jones, C. H., K. H. Mahan, and G. L. Farmer (2011), Post-Laramide Epiorogeny through Crustal Hydration?, in *AGU Fall Meeting*, edited.

Jones, C. H., J. Unruh, and L. J. Sonder (1996), The role of gravitational potential energy in active deformation in the southwestern United States, *Nature*, *381*, 37-41.

Karlstrom, K. E., et al. (2012), Surface response to mantle convection beneath the Colorado Rocky Mountains and Colorado Plateau, *Lithosphere*, *4* (1), DOI: doi: 10.1130/L150.1.

Karlstrom, K. E., S. J. Whitmeyer, K. G. Dueker, M. L. Williams, S. A. Bowring, A. Levander, E. D. Humphreys, and G. R. Keller (2005), Synthesis of results from the CD-ROM experiment: 4-D image of the lithosphere beneath the Rocky Mountains and implications for understanding the evolution of continental lithosphere, in *The Rocky Mountain region--an evolving lithosphere*, edited by K. E. Karlstrom and G. R. Keller, *AGU geophysical monograph*.

Lachenbruch, A. H., and P. Morgan (1990), Continental extension, magmatism and elevation; formal relations and rules of thumb, *Tectonophysics*, *174*, 39-62.

Levander, A., and M. S. Miller (2012), Evolutionary aspects of the lithosphere discontinuity structure in the western U.S., *G-Cubed*, *13*, DOI: 10.1029/2012GC004056.

Levander, A., B. Schmandt, M. S. Miller, K. Liu, K. E. Karlstrom, R. S. Crow, C.-T. A. Lee, and E. Humphreys (2011), Continuing Colorado plateau uplift by delamination-style convective lithospheric downwelling, *Nature*, *472*, DOI: 10.1038/nature10001.

Levander, A. R., and K. Holliger (1992), Small-scale heterogeneity and large-scale velocity structure of the continental crust, *Journal of Geophysical Research*, *97* (6), 8797-8804.

Levandowski, W. B., L. Butcher, C. H. Jones, and K. H. Mahan (*in preparation*), Cenozoic uplift of the Colorado Plateau by lithospheric removal and crustal hydration: Insight from quantitative density models, *Geology*.

Livaccari, R. F., and F. V. Perry (1993), Isotopic evidence for preservation of Cordilleran lithospheric mantle during the Sevier-Laramide Orogeny, Western United States, *Geology*, *21* (8), 719-722.

Lowry, A. R. (2012), Estimates of effective elastic thickness (Te); Surface heatflow data http://129.123.73.40/~arlowry/Data/WUS2000/README.html, accessed 10/10/2012.

Lowry, A. R., and M. Perez-Gussinye (2011), The role of crustal quartz in controlling Cordilleran deformation, *Nature*, *471*, DOI: 10.1038/nature09912.

Lowry, A. R., N. M. Ribe, and R. B. Smith (2000), Dynamic elevation of the Cordillera, western United States, *JGR*, *105* (B10), 23371-23390.

Marone, F., Y. C. Gung, and B. Romanowicz (2007), High resolution 3D radial anisotropic structure of the North American upper mantle from inversion of surface waveform data, *GJI*, *171*, DOI: 10.1111/j.1365-246X.2007.03465.x

Mooney, W., and M. K. Kaban (2010), The North American upper mantle: Density, composition, and evolution, *JGR*, *115* (B12424), DOI: 10.1029/2010JB000866.

Morgan, P. (2003), Colorado Plateau and southern Rocky Mountains uplift and erosion, in *Cenozoic systems of the Rocky Mountain region*, edited by R. G. Reynolds.

Moschetti, M. P., M. H. Ritzwoller, F. C. Lin, and Y. Yang (2010), Seismic evidence for widespread western-US deep-crustal deformation caused by extension, *Nature*, *464*, DOI: 10.1038/nature08951.

Moucha, R., A. M. Forte, D. B. Rowley, J. X. Mitrovica, G. Simmons, and S. P. Grand (2008), Mantle convection and recent evolution of the Colorado Plateau and the Rio Grande Rift Valley, *Geology*, *36* (6), 439-442, DOI: 10.1130/G24577A.

Parsons, B., and S. Daly (1983), The Relationship Between Surface Topography, Gravity Anomalies, and Temperature Structure of Convection, *J. Geophys. Res.*, *88* (B02), 1129-1144.

Parsons, T., and W. R. Thatcher (2011), Diffuse Pacific-North American plate boundary: 1000 km of dextral shear inferred from modeling geodetic data, *Geology*, *39* (10), DOI: Diffuse Pacific-North American plate boundary: 1000 km of dextral shear inferred from modeling geodetic data.

Phillips, W. S., and R. J. Stead (2008), Attenuation of Lg in the western US using the USArray, *GRL*, *35* (7), DOI: 10.1029/2007GL032926.

Prodehl, C. (1979), *Crustal structure of the western United States*, *U. S. Geol. Surv. Prof. Pap.,* vol. *1034*, 74 pp.

Pysklywec, R. N., and J. X. Mitrovica (1997), Mantle avalanches and the dynamic topography of continents, *EPSL*, *148* (3-4), DOI: 10.1016/S0012-821X(97)00045-9.

Roy, M., T. H. Jordan, and J. Pederson (2009), Colorado Plateau magmatism and uplift by warming of heterogeneous lithosphere, *Nature*, *459*, DOI: 10.1038/nature08052.

Saleeby, J. (2003), Segmentation of the Laramide Slab - evidence from the southern Sierra Nevada region, *Geological Society of America Bulletin*, *115* (6), 655-668.

Saltus, R. W., and G. A. Thompson (1995), Why is it downhill from Tonopah to Las Vegas? A case for mantle plume support of the high northern Basin and Range, *Tectonics*, *14*, 1235-1244.

Schulte-Pelkum, V., G. P. Biasi, A. F. Sheehan, and C. H. Jones (2011), Differential motion between upper crust and lithospheric mantle in the central Basin and Range, *Nature Geoscience*, *4*, DOI: 10.1038/NGEO1229.

Schutt, D., J. Buehler, K. G. Dueker, and A. R. Lowry (2011), Lithopsheric temperatures in the Western U.S., paper presented at Institute on the Lithosphere Asthenosphere Boundary, Portland, OR, Sep. 19-21, 2011.

Schutt, D., and C. E. Lesher (2010), Compositional trends among Kaapvaal Craton garnet peridotite xenoliths and their effects on seismic velocity and density, *Earth and Planetary Science Letters*, DOI: 10.1016/j.epsl.2010.10.018.

Shen, W., M. Ritzwoller, and V. Schulte-Pelkum (2013a), A 3-D Model of the Crust and Uppermost Mantle Beneath the Central and Western US by Joint Inversion of Receiver Functions and Surface Wave Dispersion, *JGR*, *118*, DOI: 10.1029/2012JB009602.

Shen, W., M. Ritzwoller, V. Schulte-Pelkum, and F. C. Lin (2013b), Joint inversion of surface wave dispersion and receiver functions: A Bayesian Monte-Carlo approach, *Geophys. J. Int.*, *192*, DOI: 10.1093/gji/ggs050.

Sigloch, K., and M. G. Mihalynuk (2013), Intra-oceanic subduction shaped the assembly of Cordilleran North America, *Nature*, *496*, DOI: 10.1038/nature12019.

SMU (2012), SMU Geothermal Laboratory surface heat flow, http://smu.edu/geothermal/georesou/DataRequest.asp, accessed 11/15/2012.

Sonder, L. J., and C. H. Jones (1999), Western United States extension: How the West was widened, *Ann. Rev. Earth Planet. Sci.*, *27*, 417-462.

Spencer, J. E. (1996), Uplift of the Colorado Plateau due to lithosphere attenuation during Laramide low-angel subduction, *Journal of Geophysical Research*, *101* (B6), 13,595-513,609.

Watts, A. B. (2001), *Isostasy and Flexure of the Lithosphere*, 458 pp., Cambridge University Press, Cambridge.

Wolf, L. W., and J. J. Cipar (1993), Through thick and thin: a new model for the Colorado Plateau from seismic refraction data from Pacific to Arizona Crustal Experiment, *Journal of Geophysical Research*, *98* (11), 19,881-819,894.

Figure Captions

Figure 1:

(a) Elevation of the western U.S., smoothed as discussed in the text. Physiographic boundaries are shown in black outline. SN: Sierra Nevada; SRP: Snake River Plain; NBR: Northern Basin and Range; SBR: Southern Basin and Range; CP: Colorado Plateau; SRM: Southern Rocky Mountains; WC: Wyoming craton; GP: Great Plains

(b) Crustal thicknesses from Shen et al. (2013a). Each of the 947 seismic stations used is marked with a small circle.

(c) Elastic thickness estimated from Lowry (2012).

Figure 2:

(a) A single member of the posterior distribution of *S*-velocity profiles for station S22A, Creede, CO.

(b) The envelope of 671 density profiles derived from (a), with random error in velocity-density conversion at each node as given by Christensen and Mooney (1995) in the crust and with 30% uncertainty in the mantle. Uncertainty is not vertically correlated.

(c) Histogram of the elevations predicted from (b). Uncertainty is 2σ.

(d) The 671 S-velocity profiles in the posterior distribution at station S22A.

(e) The envelope of densities derived from (d), with no uncertainty in velocity-density conversion.

(f) Histogram of the elevations predicted from (e). Note different mean and much larger uncertainty than (c).

(g) The envelope of densities derived from (d), but with uncertainty as in (b).

(h) Histogram of elevations predicted from (g). Note similar mean and uncertainty to (f).

Figure 3: Mantle velocity-density relationship based on purely thermal effects. At low temperatures (positive velocity perturbations relative to 4.5 km/s), the relationship is linear with a slope of 7 kg/m^3 per 1% velocity difference (~70 °C). Between 0% and -3% (~150 °C heating) velocity perturbation, anelastic effects begin to dominate, augmenting the velocity decrease for a unit temperature increase while density is still a linear function of temperature. At velocities lower than -3% (greater than 150 °C above background), we assume that material is above the solidus. Increased thermal input produces more melt, lowering velocity further, while melt has a very similar density to rock of the same temperature and thus bulk density remains constant (Hammond and Humphreys, 2000).

Figure 4:

(a) Initial estimate of mantle topography. Note large, negative values in the Wyoming Craton and Great Plains, especially when compared to the relatively constant value in the southern Rockies, Colorado Plateau, and Basin and Range.

(b) Initial estimate of crustal topography. Note large magnitude of support from the crust of the southern Rockies and Wyoming craton.

(c) Observed surface heat flow from SMU Geothermal Database. Colorscale is chosen to reflect conversion into mean crustal temperature (Figure 4d), which is described in the text.

(d) Estimated mean crustal temperature variations, based on heat flow.

(e) Topography variations arising from estimated crustal thermal structure. Note ~700 meter peak-to-trough amplitude.

(f) 2σ uncertainty in predicted elevation, derived from the envelope of acceptable velocity profiles. Mean 2σ uncertainty is 590 meters.

(g) Residual topography, H_r, as defined in eqn. 5. Negative values indicate an underestimate of density or existence of a positive downward basal normal force being exerted on the lithosphere that is not reflected in the seismic velocity. Positive values indicate upward basal normal force or density overestimate.

(h) Accepted misfit between predicted and observed topography. All values are within uncertainties shown in (f). Color scale as in (g).

Figure 5:

(a) Statistically significant residual, or H_r (Figure 4g) +/- uncertainty (Figure 4f).

(b) Minimum amount of in-situ melt, averaged through the crust that we propose contributes to H_r.

(c) Minimum amount of quartz increase, averaged through the mantle lithosphere that we propose contributes to H_r.

(d) Minimum amount of dynamic (downward) topography that we propose contributes to H_r. ~30 MPa downward normal force would produce 1 km of surface depression.

Figure 6: Components of topography. Left column is a combination of columns to the left. Top row is a combination of rows below. Same scale is used in (b), (c), (f), and (h).

(a) Flexurally smoothed topography of the western U.S.. Same as Figure 1a.

(b) Topographic variations due to thermal variations (i.e. $Hc_{thermal}$+$Hm_{thermal}$ with the mean removed to facilitate comparison). Note consistent values in Basin and Range, Snake River Plain, and Southern Rockies. Note also low values in Wyoming craton and Great Plains.

(c) Topographic variations due to compositional variations (i.e. Hc_{comp}+Hm_{comp} with the mean removed to facilitate comparison). Note very high values in the Wyoming craton, high values in the southern Rockies and Colorado Plateau, and low values in the Basin and Range.

(d) Final estimate of crustal topography, representing initial estimate (Figure 4b), corrected for the effect of proposed melt and quartz content (Figure 5b-c).

(e) Same as Figure 4e. Topography variations arising from estimated crustal thermal structure.

(f) Crustal compositional topography, representing total crustal topography (Figure 8c) corrected for estimated thermal topography of the crust (Figure 4e, 7d). Values are presented with the mean removed for more ready comparison. Note high values in the Great Plains, Rockies, and Colorado Plateau (0.5 to 2 km) as compared to the Snake River Plain and Basin and Range (<0 km).

(g) Mantle topography, same as Figure 4b.

(h) Mantle thermal topography, same as Figure 7g, but with the mean removed and then plotted on the same scale as Figures 7b, 7c, and 7f. Note large contrast between the Wyoming craton and Great Plains (values -0.5 to -1.4 km) and the Southern Rockies, Snake River Plain, Colorado Plateau and Basin and Range (nearly constant values of (0.6 to 0.85 km).

(i) Dynamic topography as in Figure 5d.

Figure 7: Bar graph of the average components of topography by province (CA=Cascades, SN=Sierra Nevada, SRP=Snake River Plain, SBR=Southern Basin and Range, GB=Great Basin/Northern Basin and Range, SRM=Southern Rocky Mountains, WC=Wyoming, HP=High Plains—smoothed elevations above 1 km, LP=Low Plains—smoothed elevations below 1 km). The minimum of each component is set to zero to better examine variations. Note similar mantle thermal topography from the Cascades through the Rockies and the strong difference between these regions and Wyoming/Plains. Other topography is mostly crustal in origin and dominated by compositional variation. Average smoothed elevation is shown in black for comparison. Misfits between predicted and observed are within uncertainty (see Figure 4h).

Figure 8: Crustal density from seismic velocities after the estimated thermal variations (Figure 4d) are removed. Note contrast between Wyoming and Southern Rockies.

Figure 9:

(a) Predicted Bouguer gravity field from our proposed density model. A correction (described in the text) is applied to mimic the effect of the Juan de Fuca slab.

(b) Observed Bouguer gravity field.

(c) Observed-predicted gravity field. 90% of the study area is matched within 40 mGal.

Figure 10: Gravitational potential energy (GPE) variations predicted from our preferred density model. Note positive GPE anomalies in the extending Northern Basin and Range (NBR) and eastern front of the Sierra Nevada (SN). Also note negative GPE along the western margin of North America, especially in the Cascades Forearc, with an arm of

negative GPE extending eastward at the latitude of the Yakima Fold and Thrust Belt (YFTB).

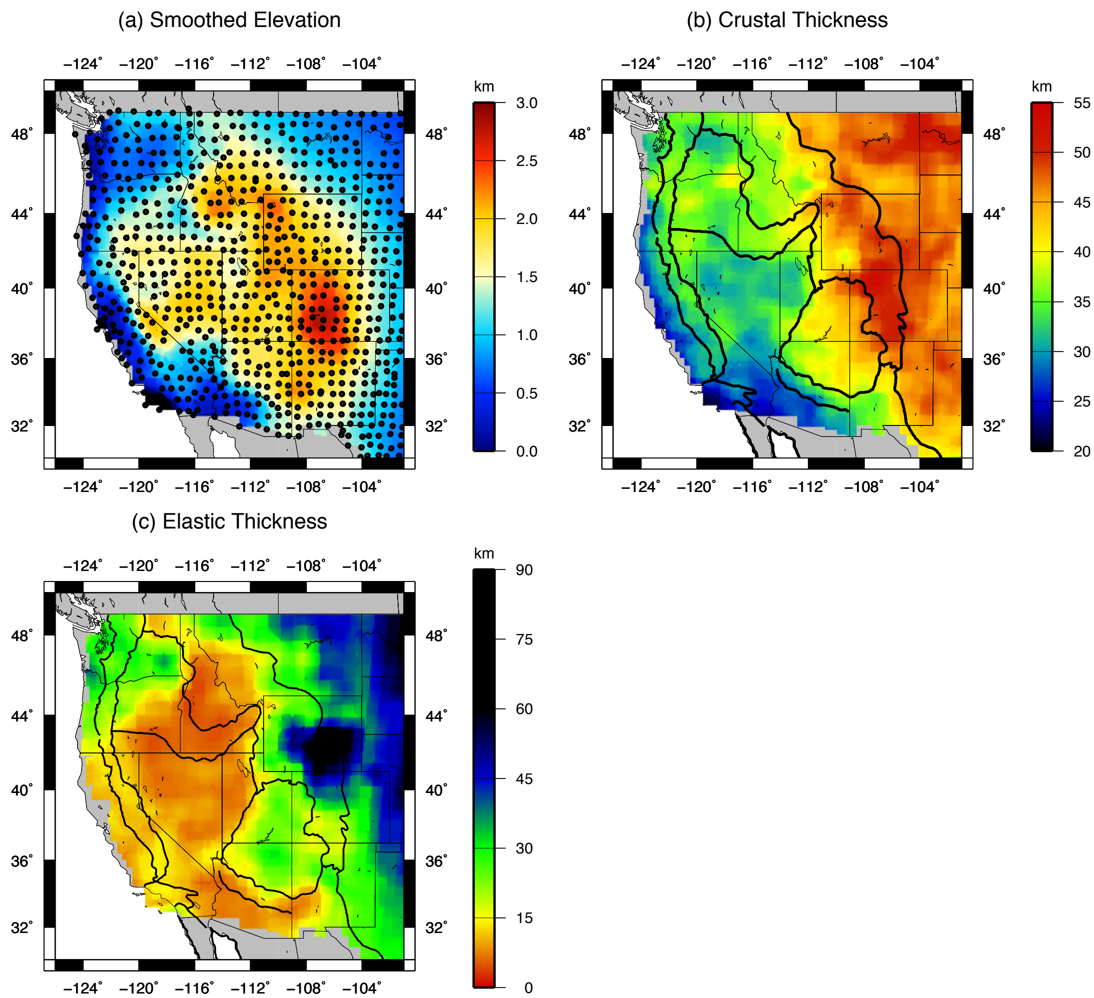

1079

1080 Figure 1

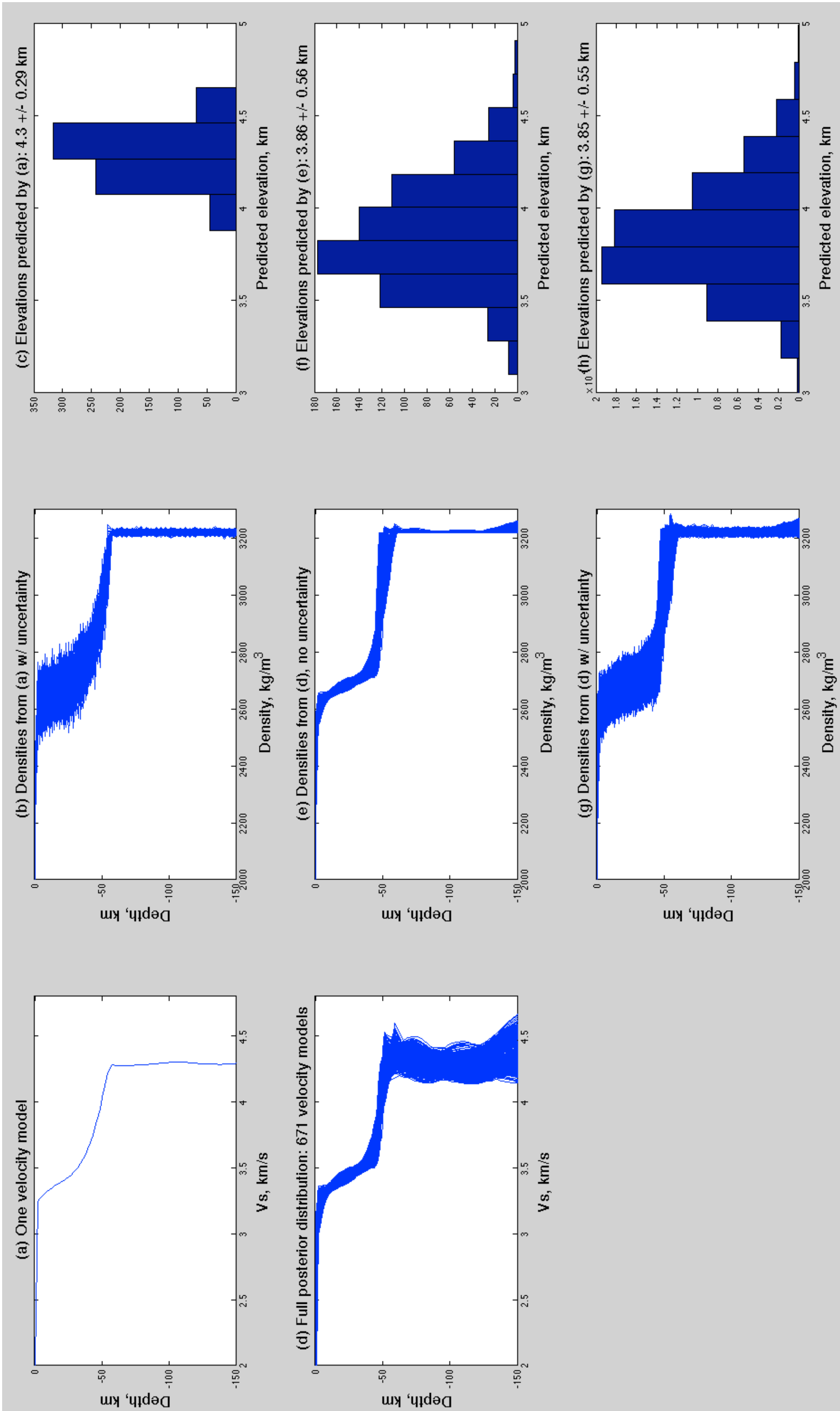
(a) One velocity model
Depth, km
Vs, km/s
(b) Densities from (a) w/ uncertainty
Density, kg/m3
(c) Elevations predicted by (a): 4.3 +/- 0.29 km
Predicted elevation, km
(d) Full posterior distribution: 671 velocity models
(e) Densities from (d), no uncertainty
(f) Elevations predicted by (e): 3.86 +/- 0.56 km
(g) Densities from (d) w/ uncertainty
(h) Elevations predicted by (g): 3.85 +/- 0.55 km

Figure 2

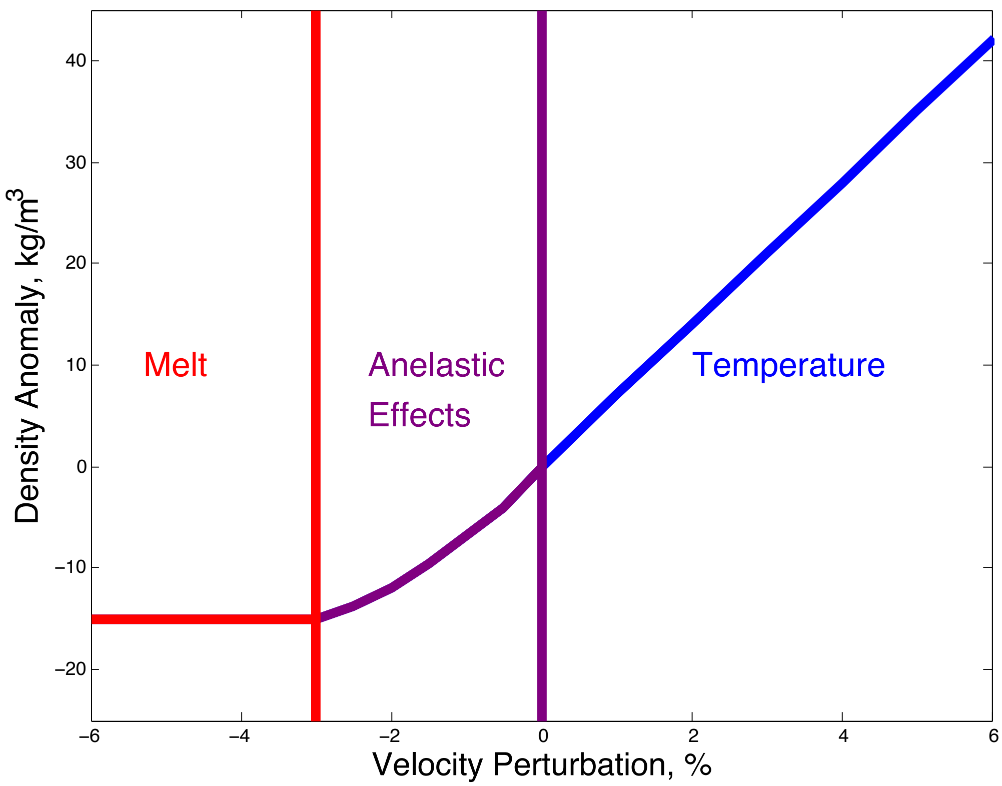
Melt
Anelastic
Effects
Temperature
Density Anomaly, kg/m3
Velocity Perturbation, %
40
30
20
10
0
−10
−20
−6
−4
−2
0
2
4
6

Figure 3

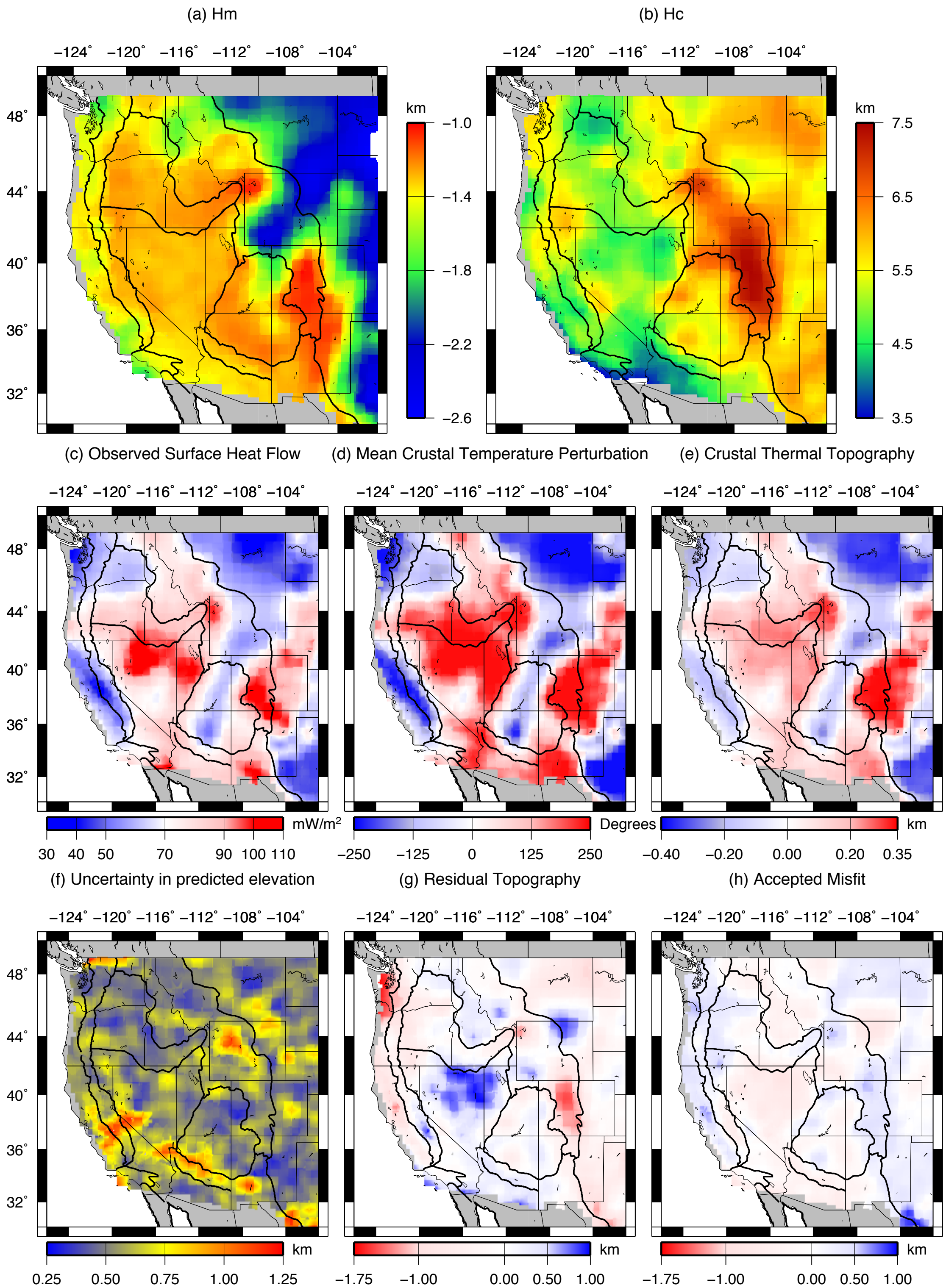
(a) Hm
(b) Hc
−124° −120° −116° −112° −108° −104°
48° 44° 40° 36° 32°
km
−1.0 −1.4 −1.8 −2.2 −2.6
km
7.5 6.5 5.5 4.5 3.5
(c) Observed Surface Heat Flow
(d) Mean Crustal Temperature Perturbation
(e) Crustal Thermal Topography
mW/m²
30 40 50 70 90 100 110
Degrees
−250 −125 0 125 250
km
−0.40 −0.20 0.00 0.20 0.35
(f) Uncertainty in predicted elevation
(g) Residual Topography
(h) Accepted Misfit
km
0.25 0.50 0.75 1.00 1.25
km
−1.75 −1.00 0.00 0.50 1.00
km
−1.75 −1.00 0.00 0.50 1.00

Figure 4

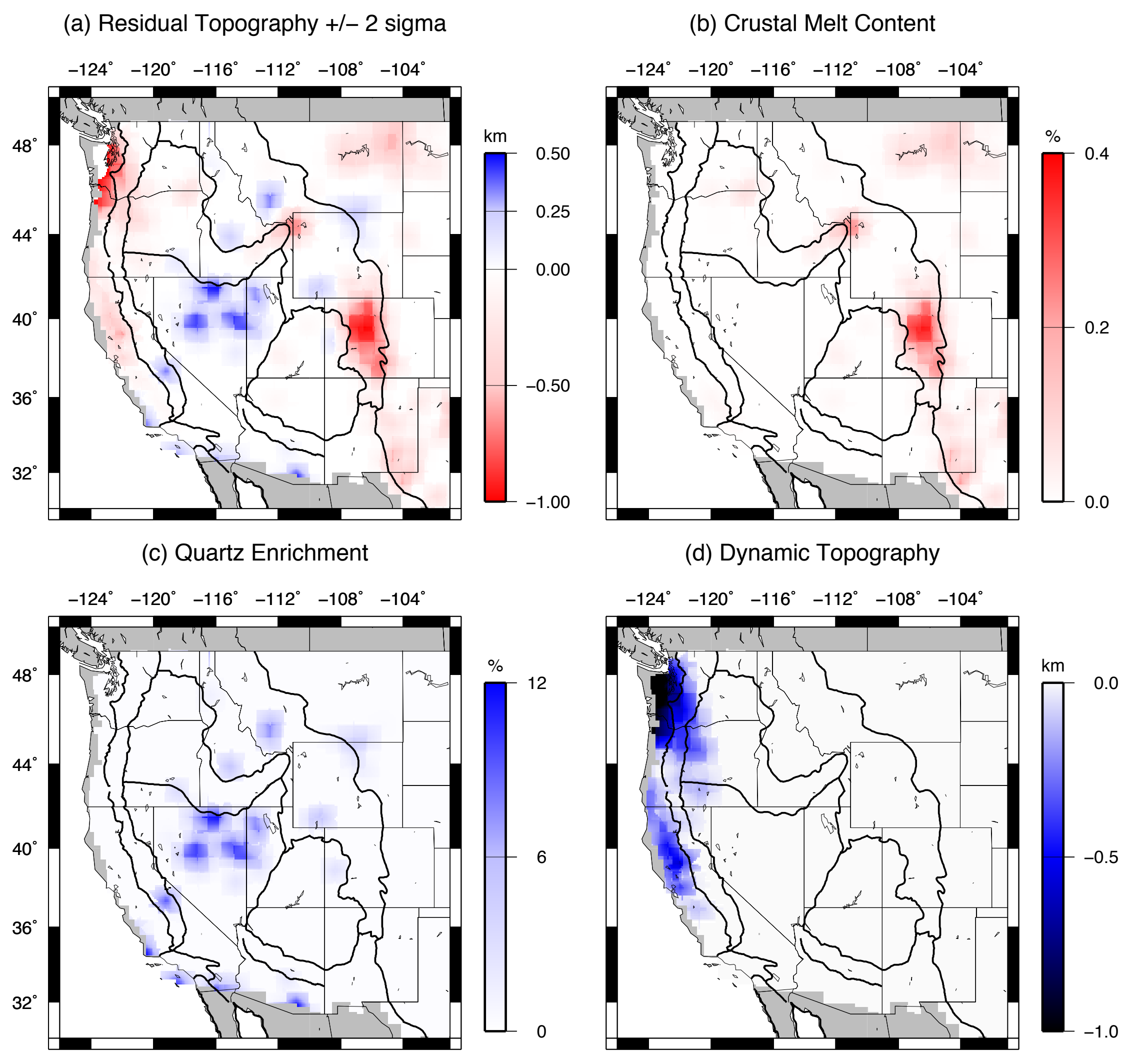

1087

1088 Figure 5

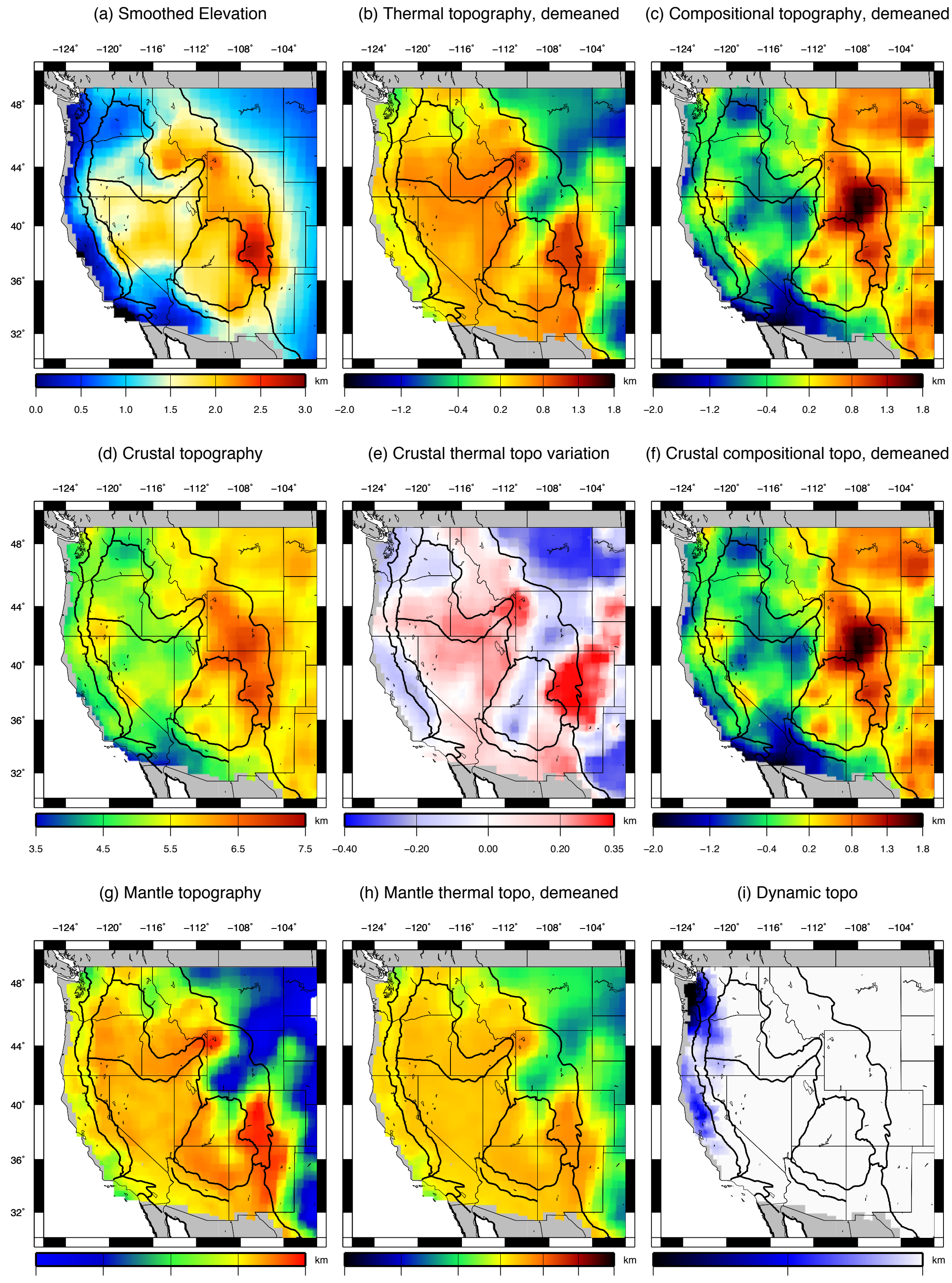
(a) Smoothed Elevation
(b) Thermal topography, demeaned
(c) Compositional topography, demeaned
(d) Crustal topography
(e) Crustal thermal topo variation
(f) Crustal compositional topo, demeaned
(g) Mantle topography
(h) Mantle thermal topo, demeaned
(i) Dynamic topo
−124° −120° −116° −112° −108° −104°
48° 44° 40° 36° 32°
km
0.0 0.5 1.0 1.5 2.0 2.5 3.0
−2.0 −1.2 −0.4 0.2 0.8 1.3 1.8
3.5 4.5 5.5 6.5 7.5
−0.40 −0.20 0.00 0.20 0.35
−2.6 −2.2 −1.8 −1.4 −1.0
−1.0 −0.5 0.0

Figure 6

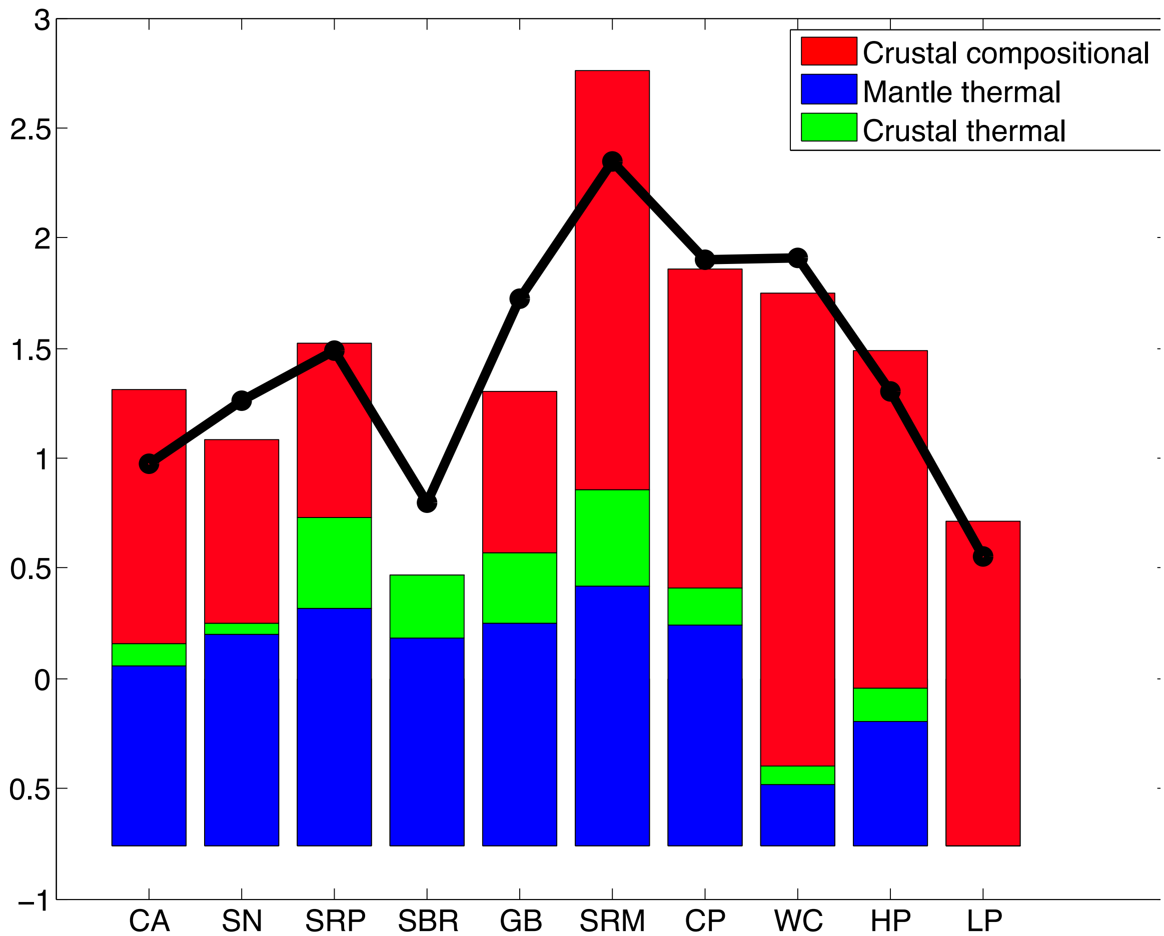
Crustal compositional
Mantle thermal
Crustal thermal
3
2.5
2
1.5
1
0.5
0
0.5
−1
CA
SN
SRP
SBR
GB
SRM
CP
WC
HP
LP

Figure 7

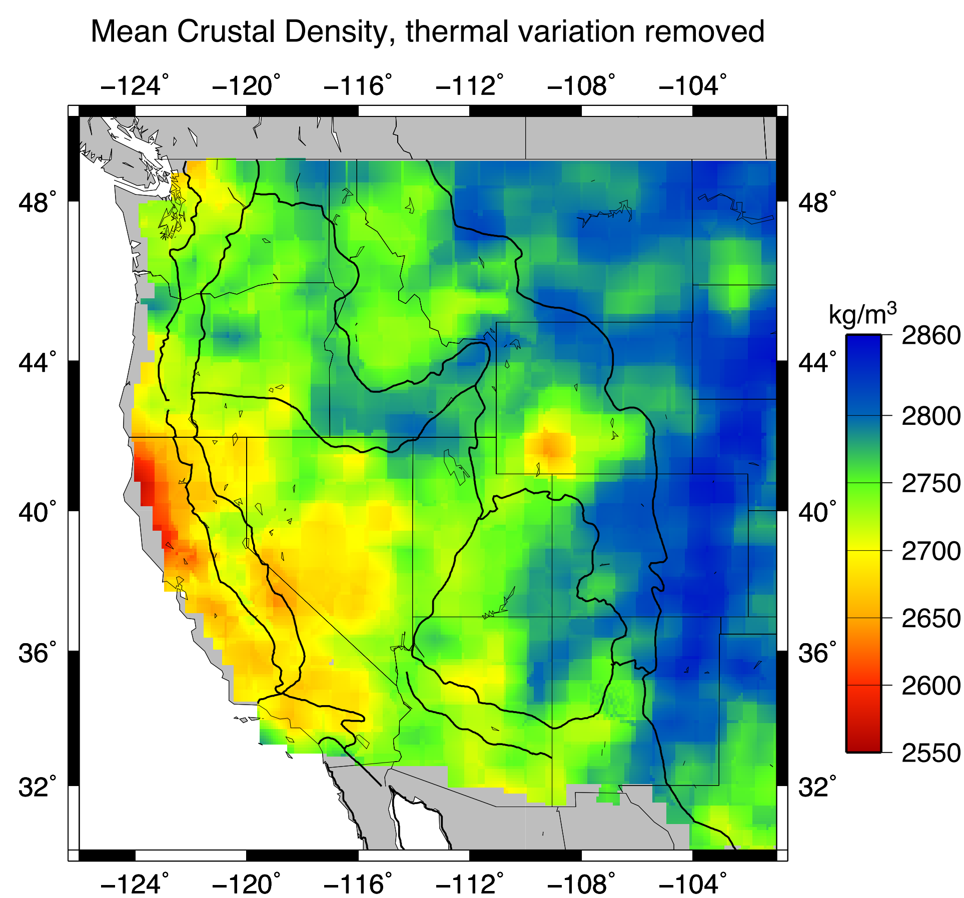
Mean Crustal Density, thermal variation removed
−124˚
−120˚
−116˚
−112˚
−108˚
−104˚
48˚
44˚
40˚
36˚
32˚
kg/m3
2860
2800
2750
2700
2650
2600
2550

Figure 8

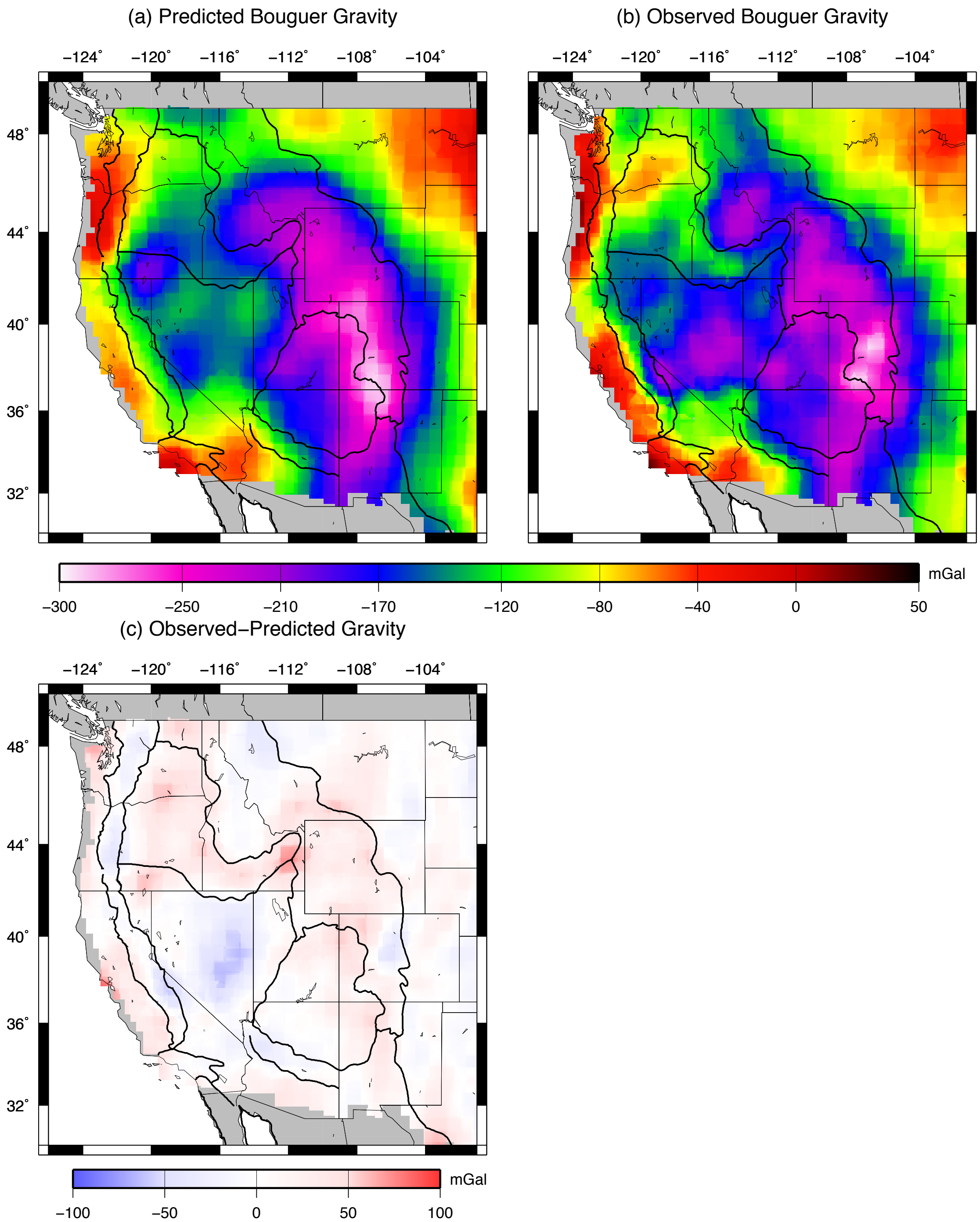
(a) Predicted Bouguer Gravity
(b) Observed Bouguer Gravity
–124˚ –120˚ –116˚ –112˚ –108˚ –104˚
48˚ 44˚ 40˚ 36˚ 32˚
mGal
–300 –250 –210 –170 –120 –80 –40 0 50
(c) Observed–Predicted Gravity
mGal
–100 –50 0 50 100

Figure 9

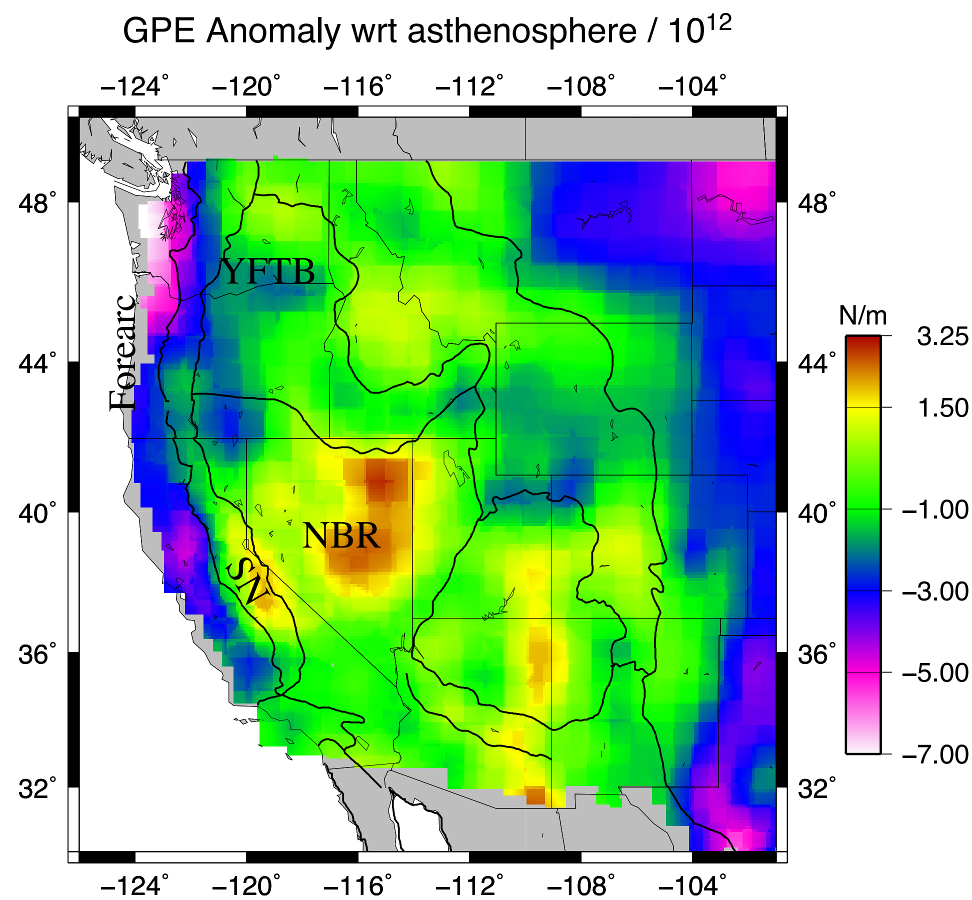

1098

1099 Figure 10